AD-A173 762 VORTEX-AIRFOIL INTERACTION AND APPLICATION OF METHODS FOR DIGITAL FRINGE.. (U) MAX-PLANCK-INST FUER STROEMUNGSFORSCHUNG GOETTINGEN (GERMANY F.. 1/1

UNCLASSIFIED G E MEIER ET AL. 15 MAR 86 R/D-3037-AN F/G 20/1 NL

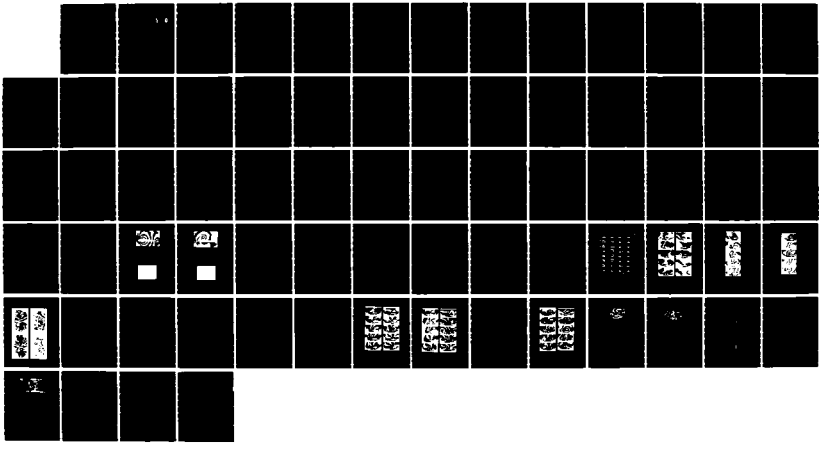

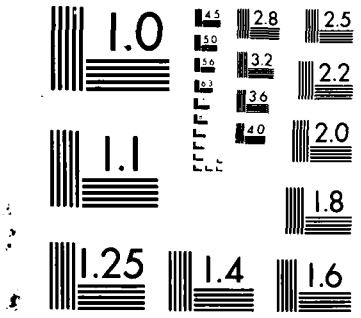

VORTEX-AIRFOIL INTERACTION AND APPLICATION OF METHODS FOR DIGITAL FRINGE ANALYSIS

Principal Investigator: Dr. G. E. A. Meier

Contractor: Professor Dr. E.-A. Müller
Max-Planck-Institut
für Strömungsforschung
D-3400 Göttingen, Bunsenstraße 10
Federal Republic of Germany

Final Technical Report

March 15, 1986

Contract Number DAJA 37-81-C-0251

The research reported in this document has been made possible through the support and sponsorship of the U.S. Goverment through its EUROPEAN RESEARCH OFFICE OF THE U.S. ARMY. ~~This report is intended only for the internal management use of the Contractor and the U.S. Goverment.~~

Table of Contents

UNCLASSIFIED

SECURITY CLASSIFICATION OF THIS PAGE (When Data Entered)

R&D 3037-AN

REPORT DOCUMENTATION PAGE		READ INSTRUCTIONS BEFORE COMPLETING FORM
1. REPORT NUMBER	2. GOVT ACCESSION NO. AD-A173 762	3. RECIPIENT'S CATALOG NUMBER
4. TITLE (and Subtitle) Vortex-airfoil interaction and application of methods for digital fringe analysis.		5. TYPE OF REPORT & PERIOD COVERED
		6. PERFORMING ORG. REPORT NUMBER
7. AUTHOR(s) Dr. G.E.A. Meier; Dipl. Phys. R. Wenskus; Dipl. Phys. H.-M. Lent		8. CONTRACT OR GRANT NUMBER(s) DAJA 37-81-C-0251
9. PERFORMING ORGANIZATION NAME AND ADDRESS MPI für Strömungsforschung D-3400 Göttingen Böttingerstr. 4-8		10. PROGRAM ELEMENT, PROJECT, TASK AREA & WORK UNIT NUMBERS 6.11.02A 1T16 1102BH57-06
11. CONTROLLING OFFICE NAME AND ADDRESS USARDSG-UK Box 65, FPO New York 09510		12. REPORT DATE
		13. NUMBER OF PAGES
14. MONITORING AGENCY NAME & ADDRESS (if different from Controlling Office)		15. SECURITY CLASS. (of this report) Unclassified
		15a. DECLASSIFICATION/DOWNGRADING SCHEDULE

16. DISTRIBUTION STATEMENT (of this Report)

Approved for public release; distribution unlimited

17. DISTRIBUTION STATEMENT (of the abstract entered in Block 20, if different from Report)

18. SUPPLEMENTARY NOTES

19. KEY WORDS (Continue on reverse side if necessary and identify by block number)

transonic noise generation, boundary layer, airfoil-vortex interaction, secondary vortex, vortex noise, digital interferogram analysis, fringe evaluation, image processing

20. ABSTRACT (Continue on reverse side if necessary and identify by block number)

The interaction of convected vortices with different airfoils was investigated in a duct and a shock tube flow. Different kinds of separation and secondary vortex generation have a governing influence on airfoil-vortex interaction. Steep sound waves propagating upstream are generated at the leading edge. A system for digital processing of flow interferograms has been developed.

DD FORM 1 JAN 73 1473 EDITION OF 1 NOV 65 IS OBSOLETE

UNCLASSIFIED

1. Introduction

The aim of this project is to investigate vortex-profile interaction. Vortex interaction with solid walls generates sound. Vortex noise occurs nearly everywhere in aerodynamics and especially it is one of the helicopter noise sources.

There is lack of knowledge about the near-field flow at the profile. Theoretical considerations are difficult, because the role of the Kutta-Condition is not understood and the full Navier-Stokes equations are not easy to solve. Thus experiments must be carried out. After some considerations about vortex paths with the method of conformal mapping, the first step into the problem was an experiment which gave an overview on the phenomena occurring. In a transonic tunnel a profile was placed in the wake of a vortex shedding cylinder. The interaction of the Karman vortex street and the profile can be measured by pressure transducers and high speed interferograms. Pressure waves and flow pattern can be evaluated from these experiments.

Additionally, for single vortex interaction a shock tube experiment was performed. Single starting vortices are generated with an additional airfoil. The boundary layer is very thin in this case. So the vortices are similar to potential vortices. These experiments allow comparisons to the theoretical results achieved with the method of conformal mapping.

2. A model for vortex paths around a profile and the sound generated by by vortex-profile interaction

Following the work of Obermeier, the path of a cylinder vortex around a Joukowsky profile is calculated according to potential theory without taking into account the Kutta condition. Sound generation is calculated by matched asymptotic expansions [1,2,3].

The flow potential of vortex-profile interaction

Potential flow of a vortex near a wall is described by two mirror vortices in the complex u-plane. The plane of symmetry corresponds to the wall.

$$\phi_u = \frac{-j\,\Gamma}{2\pi}\left(\log(u-u_o) - \log(u+\bar{u}_o)\right)$$

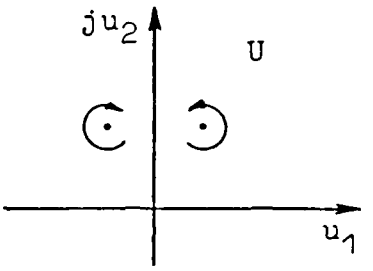

Using the rational function

$$v = \frac{u+1}{u-1} \qquad u = \frac{v+1}{v-1}$$

the imaginary axis is mapped to the unit circle in the v-plane. One gets the potential of flow of a vortex near a cylinder

$$\phi_v = \frac{-j\,\Gamma}{2\pi}\left(\log\left(\frac{v+1}{v-1} - \frac{v_o+1}{v_o-1}\right) - \log\left(\frac{v+1}{v-1} + \frac{\bar{v}_o+1}{\bar{v}_o-1}\right)\right)$$

A free stream U_0 and an additional value of circulation around the origin are added to this potential; circulation around the cylinder is thus eliminated and the Kutta condition is satisfied when the vortex is far away.

$$\phi_v = \frac{-j\,\Gamma}{2\pi}\left(\log\left(\frac{v+1}{v-1} - \frac{v_o+1}{v_o-1}\right) - \log\left(\frac{v+1}{v-1} + \frac{\bar{v}_o+1}{\bar{v}_o-1}\right) + \log v\right)$$

$$+ U_o\left(v + \frac{1}{v}\right)$$

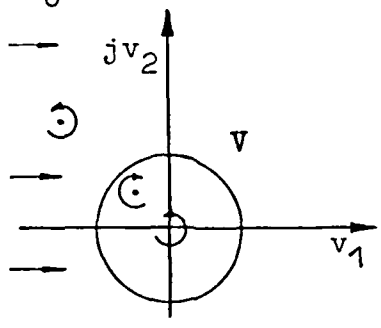

As a preparation for the Joukowsky map, the radius of the circle is enlarged by a factor (a+b) and the center is translated by an amount a. The width of the profile depends on the parameter a, the roundness of the trailing edge on b.

$$w = (a+b)v - (a-1) \qquad v = \frac{w+a-1}{a+b}$$

$$\phi_w = \frac{-j\,\Gamma}{2\pi}\left(\log\left(\frac{w+2a+b-1}{w-b-1} - \frac{w_o+2a+b-1}{w_o-b-1}\right) -\right.$$

$$\left.\log\left(\frac{w+2a+b-1}{w-b-1} + \frac{\bar{w}_o+2a+b-1}{\bar{w}_o-b-1}\right) + \log\frac{w+a-1}{a+b}\right) + U_o\left(\frac{w+a-1}{a+b} + \frac{a+b}{w+a-1}\right)$$

Using the Joukowsky transform

$$z = \frac{1}{2}\left(w + \frac{1}{w}\right) \qquad w = z + z\cdot\sqrt{1 - \frac{1}{z^2}}$$

one gets a wing profile which approximates standard symmetrical profiles except for its rounded trailing edge when the parameters a and b are chosen appropriately. For the complex root the convention

$$\mathrm{Re}\left(\sqrt{1-\frac{1}{z^2}}\right) \geq 0$$

is used in the following.

New functions A, B and C are introduced to simplify notation:

$$B(z) := z+z\sqrt{1-\frac{1}{z^2}} \qquad A(z) := \frac{B(z)+2a+b-1}{B(z)-b-1} \qquad C(z) := \frac{B(z)+a-1}{a+b}$$

$$\phi_z = \frac{-j\Gamma}{2\pi}\left(\log\frac{A(z)-A(z_0)}{A(z)+A(\overline{z}_0)} + \log C(z)\right) + U_0\left(C(z)+\frac{1}{C(z)}\right)$$

Note that the velocity at infinity now is given by $U_\infty = 2\,U_0/(a+b)$.

As a next step the nondimensional variable $z_1 := z/l_1$ is introduced. (The index 1 will be suppressed for the sake of simplicity). The length of the profile equals

$l = a+b + (a+b)/((b+1)(2a+b-1))$.

Introducing the parameter

$c := 1 + 1/((b+1)(2a+b-1))$

und using the coefficient of circulation

$Z := 2\Gamma/(U_\infty\, l)$

we get the nondimensional potential

$$\phi = \frac{-j}{2\pi}\left(\log\frac{A(z)-A(z_0)}{A(z)+A(\overline{z}_0)} + \log C(z)\right) + \frac{1}{cZ}\left(C(z)+\frac{1}{C(z)}\right)$$

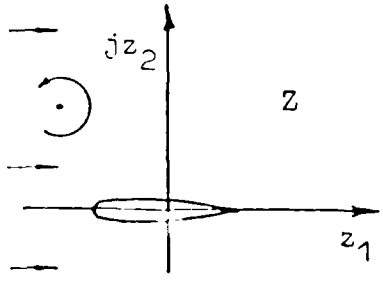

The potential of a vortex near a profile may be written in a somewhat different form:

$$\tilde{\phi} = \frac{-j}{2\pi}\left(\log \frac{B(z) - B(z_o)}{B(z)+a-1-\frac{a+b}{C(\overline{z}_o)}} + \log C(z) \right) + \frac{1}{cZ}\left(C(z) + \frac{1}{C(z)}\right)$$

which is achieved by mapping the cylinder potential

$$\tilde{\phi}_v = \frac{-j\Gamma}{2\pi}\left(\log \frac{v - v_o}{v - \frac{1}{\overline{v}_o}} + \log v \right) + U_o\left(v + \frac{1}{v} \right)$$

$$= \phi_v + \frac{j\Gamma}{2\pi} \log \frac{\overline{v}_o(v_o-1)}{-(\overline{v}_o-1)}$$

Besides this complex representation, a polar coordinate representation using real functions has been described in the literature. Walton [4] used such a representation for the case of a cylinder and Lin [5] for a flat plate.

The potential used in this work does not satisfy the Kutta condition when the vortex is near the profile. This deficiency can be corrected by matching the inner circulation and allowing vortices to be generated at the trailing edge. However, this method encounters difficulties because chaotic behaviour may appear when many free vortices are present.

Parthasarathy [6] avoids this difficulty by imposing restricting conditions: the vortices generated at the trailing edge swim off horizontally and with the velocity of the surrounding fluid.

As the author does not know of a method not imposing restricting conditions, the Kutta condition has not been taken into account in this work. This approach may be justified as it is not known whether, and if so, in which way the Kutta condition is satisfied in a high frequency regime, for example when vortices are passing nearby.

The path of a vortex

The movement of a vortex can be deduced from the translational velocity at the location of the vortex core. This velocity is calculated by a limit process: the rotational velocity near the vortex core is subtracted from the total velocity. The following expressions are valid for the conjugated velocity of the core:

$$\frac{d\bar{z}_o}{dt} = \lim_{d\to 0}\left[\left(\frac{d\phi}{dz}\right)_{z=z_o+d} + \frac{j}{2\pi}\,\frac{1}{d}\right]$$

$$= \lim_{d\to 0}\left[\frac{-j}{2\pi}\cdot\left(\frac{A'(z_o+d)}{A(z_o+d)-A(z_o)} - \frac{A'(z_o+d)}{A(z_o+d)+A(\bar{z}_o)} - \frac{1}{d} + \frac{C'(z_o)}{C(z_o)}\right)\right.$$

$$\left. + \frac{1}{cZ}\left(C'(z_o) - \frac{C'(z_o)}{C(z_o)^2}\right)\right]$$

$$= \lim_{d\to 0}\left[\frac{-j}{2\pi}\cdot\left(\frac{A'(z_o)+dA''(z_o)+O(d^2)}{d(A'(z_o)+\frac{d}{2}A''(z_o)+O(d^2))} - \frac{1}{d} - \frac{A'(\bar{z}_o)}{A(z_o)+A(\bar{z}_o)}\right.\right.$$

$$\left.\left. + \frac{C'(z_o)}{C(z_o)}\right) + \frac{1}{cZ}\left(C(z_o) - \frac{C'(z_o)}{C(z_o)^2}\right)\right]$$

$$= \frac{-j}{2\pi}\cdot\left(\frac{A''(z_o)}{2A'(z_o)} - \frac{A'(\bar{z}_o)}{A(z_o)+A(\bar{z}_o)} + \frac{C'(z_o)}{C(z_o)}\right) + \frac{1}{cZ}\left(C'(z_o) - \frac{C'(z_o)}{C(z_o)^2}\right)$$

The derivatives of the functions A, B and C are given by:

$$A'(z) = \frac{-2(a+b)B(z)}{(B(z)-b-1)^2 \cdot z \cdot \sqrt{1-\frac{1}{z^2}}} \qquad C'(z) = \frac{B'(z)}{a+b}$$

$$B'(z) = \frac{B(z)}{z \cdot \sqrt{1-\frac{1}{z^2}}} \qquad A''(z) = 2(a+b)\,\frac{2B(z)^2 z\sqrt{1-\frac{1}{z^2}} + B(z)-b-1}{(B(z)-b-1)^3 \cdot z^3 \cdot (1-\frac{1}{z^2})^{3/2}}$$

An elegant method of calculation uses a Hamiltonian

$$\frac{d\bar{z}_o}{dt} =: \frac{\partial H}{\partial z_o} \qquad \frac{dz_o}{dt} =: -\frac{\partial H}{\partial \bar{z}_o}$$

$$H = \frac{-j}{2\pi} \cdot \left(\frac{1}{2} \log(A'(z_o)A'(\bar{z}_o)) - \log(A(z_o)+A(\bar{z}_o)) + \log(C(z_o)C(\bar{z}_o)) \right)$$

$$+ \frac{1}{cZ}\left(C(z_o) - C(\bar{z}_o) + \frac{1}{C(z_o)} - \frac{1}{C(\bar{z}_o)} \right)$$

The function H is a constant of motion [3,5,7]. This facilitates the control of accuracy when evaluating the differential equation numerically. Evaluation is done by the Runge-Kutta method. Figure 1a shows 6 vortex paths around a flat plate. The coefficient of circulation is 10, the vortices are rotating counterclockwise. The length of the strokes corresponds to the unit of time. There are closed paths around the profile and beneath it. Other calculations [8,9] show that vortex trapping is possible, too.

The far field

When $z = z_0(t)$ is known, the hydrodynamic far field can be calculated:

$$\lim_{|z|\to\infty} A(z) = 1 + \frac{a+b}{z} + O\left(\frac{1}{z^2}\right) \qquad \lim_{|z|\to\infty} C(z) = \frac{2z - \frac{1}{2z}}{a+b} + O\left(\frac{1}{z^2}\right) + \text{Konst.}$$

$$\lim_{|z|\to\infty} \phi(z) = \frac{-j}{2\pi}\left(\log\left(1 + \frac{a+b}{z} - A(z_0)\right) - \log\left(1 + \frac{a+b}{z} + A(\overline{z}_0)\right)\right.$$

$$\left. + \log\frac{2z - \frac{1}{2z}}{a+b}\right) + \frac{1}{cZ}\left(\frac{2z - \frac{1}{2z}}{a+b} + \frac{a+b}{2z}\right) + O\left(\frac{1}{z^2}\right) + \text{Konst.}$$

$$= \frac{-j}{2\pi}\left(\frac{a+b}{z}\left(\frac{1}{1 - A(z_0)} - \frac{1}{1 + A(\overline{z}_0)}\right) + \log\frac{2z - \frac{1}{2z}}{a+b}\right)$$

$$+ \frac{2}{cZ(a+b)}\left(z + \frac{(a+b)^2 - 1}{4z}\right) + O\left(\frac{1}{z^2}\right) + \text{Konst.}$$

Let $\tau := \frac{\Gamma}{l_i^2} t$ be the nondimensional time and

$p_i := p \frac{l_i^2}{\Gamma^2 \rho}$ the nondimensional pressure.

p_i obeys the relation $P_i = -\left(\frac{\partial \phi}{\partial \tau} + \frac{1}{2}|\nabla \phi|^2\right)$

Let Ψ be the stream function of the far field approximation of

$$-\frac{i\Gamma}{2\pi} \log\frac{A(z) - A(z_0)}{A(z) + A(\overline{z}_0)}$$

$$\psi(z_0(\tau)) = (a+b)\left(\frac{1}{1 - A(z_0)} - \frac{1}{1 + A(\overline{z}_0)}\right)$$

Then it follows for the derivative

$$\frac{\partial \Psi}{\partial \tau} = (a+b)\left(\frac{A'(z_o)\cdot \dot{z}_o}{(1 - A(z_o))^2} + \frac{A'(\overline{z_o})\cdot \dot{\overline{z}}_o}{(1 + A(\overline{z_o}))^2} \right)$$

$$= \frac{1}{2}\left(B'(z_o)\cdot \dot{z}_o + \frac{B'(\overline{z_o})}{C(\overline{z_o})^2}\cdot \dot{\overline{z}}_o \right)$$

Furthermore,

$$\lim_{|z|\to\infty} |\nabla\phi|^2 = \left| \left(\frac{2}{cZ(a+b)} \right)^2 - \frac{j}{2\pi}\frac{4}{cZ(a+b)}\frac{1}{z} + O\left(\frac{1}{z^2}\right) \right|$$

$$= \left(\frac{2}{cZ(a+b)} \right)^2 - \mathrm{Re}\left(\frac{4j}{2\pi cZ(a+b)}\frac{1}{z} \right) + O\left(\frac{1}{z^2}\right)$$

is valid.

The pressure in the far field can be expressed in terms of dipole moments:

$$P_i = -\left(\frac{\partial\phi}{\partial\tau} + \frac{1}{2}|\nabla\phi|^2 \right) =: \frac{\overrightarrow{-z}}{|z|^2}\left(m_1 + jm_2 \right) + \text{Konst.}$$

with

$$m_1 = \frac{1}{2\pi}\,\mathrm{Re}\left(\frac{\partial\Psi}{\partial\tau}\right) \qquad m_2 = \frac{1}{2\pi}\,\mathrm{Im}\left(\frac{\partial\Psi}{\partial\tau} - \frac{2j}{cZ(a+b)} \right)$$

Figure 16 shows 6 vortex paths near a Joukowsky profile. The parameters were chosen in such a way that the profile approximates a NACA 0012 as has been used in the experiments. The coefficient of circulation is 1.

Obermeier used matched asymptotic expansions to fit an acoustic field to the hydrodynamic far field. A detailed description of this method can be found in [1,2,3,10,11].

Using nondimensional coordinates for the inner (index i) and outer (index a) range

$$\varepsilon = \frac{\Gamma}{l_i a_o} \qquad z = l_i z_i = l_i \frac{z_a}{\varepsilon} \qquad M = \frac{U_\infty}{a_o}$$

and transforming to the coordinates

$$z_a = (x_a, y_a) \qquad x^a = \frac{x_a}{\sqrt{1 - M^2}} \qquad y^a = y_a \qquad T = \frac{\tau + M(x_a - M\tau)}{\sqrt{1 - M^2}}$$

$$(x^a, y^a) = [R^a, \varphi]$$

one gets the following result for the sound pressure:

$$\lim_{R^a \to \infty} p_1^a = \frac{-\frac{\varepsilon}{2\pi}}{1 + M\cos\varphi} \int_{-\infty}^{\infty} \omega^2 F_2(\omega) H_1^{(1)}(\omega R^a) e^{-j\varphi^a - j\omega T} d\omega$$

$H_1^{(1)}$ being the Hankel function of first type and order one, which is the solution for a dipol-like cylindrical sound field. Besides a constant factor, $F_2(\omega)$ is the Fourier transform of $\psi(\tau)$

$$F_2(\omega) = \frac{-j}{4} \int_{-\infty}^{+\infty} \psi(\tau) \; e^{j\omega\tau} \; d\tau$$

3. Experimental Facilities

3.1. Duct, Vortex Generators and Profiles

The transonic duct (Fig. 2) is a vacuum type wind tunnel with two vacuum tanks of 132 m^3 and 24 m^3 volume [12]. The maximum measuring time for the profile investigation arrangement is 10 s at Mach 1 and 25 s at Mach 0.3. A new experiment can be performed every 4 minutes (this is the time the pump needs to evacuate the tanks).

Air is sucked in from the laboratory or an air drying unit. The velocity in the measuring chamber is controlled by an adjustable diffuser. In the smallest cross section of the diffuser the air reaches Mach 1, so there is constant velocity throughout the measuring time. The velocity of the air can be chosen from v=0 to v=600 m/s if a Laval nozzle is used.

The test section of the duct (Fig. 6) is 800 mm long, 330 mm high and 100 mm wide. The upper and the lower side of the chamber have slots to provide good acoustical damping. The vortex generators are installed in the 200 mm front section (6a,c,e) or at locations nearer to the window (6b,d). The profile can be mounted between the windows downstream of the generators. The windows have a diameter of 230 mm and have interferometric quality. Instead of the windows a pressure measuring plate with an array of holes at 15 mm distance can be used. The signals of up to 16 Kulite transducers can be digitized simultaneously. Thus accurate pressure field recordings can be made.

Two profiles are used for the investigations. They have a NACA 0012 shape with 120 mm and 60 mm chord length, respectively. For the investigations they are placed between the windows at different angles of attack.

Different kinds of bluff bodies are used as vortex generators. Their wake is a Karman vortex street consisting of strong vortices of opposite sense of direction. The frequency of the vortices depends on the size and shape of the bluff body (a circular cylinder has a nearly constant Strouhal

number of 0.2; i.e. the distance between vortices of equal sense of direction is 5 diameters). Several bluff body shapes were investigated, it turned out that a square cylinder has the highest amplitudes and best constancy of Strouhal frequencies over the Reynolds number range from 0.1 up to 0.5 millions.

3.2. Shock Tube

Like other authors [13] we have used a shock tube to generate starting vortices. The shock tube consists of a high pressure section of 2100 mm length and a low pressure section of 3700 mm (fig. 7). The width of the tube is 100 mm and the height is 330 mm (fig. 8). The distance from the membrane to the measuring chamber divided by width and height of the tube give length to width and length to height ratios of 27 and 8.

The bottom and the top of the low pressure section are rounded with a diameter of 100 mm to prevent shock disturbances (fig. 8). The measuring chamber is the same as in the wind tunnel experiment (fig. 9). The same measuring devices can be used. The low pressure section is evacuated by the wind tunnel vacuum tank to a vacuum up to 100 mbar. The high pressure section is pressurized up to 1500 mbar. Pressure ratios from 1 up to 15 can be obtained.

Figure 8 shows the measuring chamber. A GOE 508 profile of 120 mm chordlength is mounted before the window area. The GOE 508 profile is a high lift profile with flat underside. It is mounted at an angle of 7.5 degrees. Its stationary lift coefficient is 1.25. 5 mm of the trailing edge of the profile are visible in the viewing field. The 60 mm NACA 0012 profile is mounted 38 mm apart at the same height as the trailing edge of the asymmetric profile.

3.3. Computer Installation

The computer is a PDP 11/34. It has connections to the image processing computer, also a PDP 11/34, to the institute computer, a VAX, and to the central computer of Göttingen University and Max-Planck-Institute, a Uni-

vac 1108. Figure 4 shows the configuration of the PDP and the periphery [14].

On the right are the data aquisition components. A Camac crate controller (CA11-FP,Digital Equipment) is the interface to 16 transient recorders (Le Croy), a real time clock and a digital I/O port. The transient recorders have 8 K storage capacity of 10 bit data at data aquisition rates of up to 1 MHz. They are used to record the pressure data.

An IEC-bus interface is used to record the static pressure with the help of a digital voltmeter.

The third I/O component is the controller (LPA11-K, Digital Equipment) of a 12 bit analog/digital converter. Data rates up to 50 KHz can be stored directly on the disc.

The storage of measured data is performed with a 160 Megabyte disc (System Industries). Long term storage is done with a magtape.

Fast data processing is done with the array processor (Floating Point Systems). It is well suited for fast Fourier transforms, a FFT of 1024 points is done in 3 ms.

For visualisation of data there graphic terminals (VT100 and Tektronix) and a hard copy unit, connected to the computer by a terminal multiplexer.

The interface to the fast data line to the image processing computer is a DRU-11C (Digital Equipment). A DMC-11 is the interface to the data line to the VAX and Univac. The VAX is used for program development and other computing purposes. The Univac is needed for DISSPLA plots.

3.4. Optical Facility

A Zeiss Mach-Zehnder interferometer can be used for optical investigations (fig. 3). The channel width is 100 mm. Vacuum in the measuring chamber corresponds to 48 whole fringes in interferograms. The light source is a high

frequency spark light source. Movies can be made with a rotating drum camera at 10 Khz or with a Fastax camera at speeds up to 8 Khz.

4. Testing of the Experimental Arrangement

4.1. Vortex Street Generators

Vortex streets should be two-dimensional, should have a constant Strouhal number and must consist of strong potential vortices of the right spacing to be of use in our experiment. The interaction of vortices among themselves should be less than the interaction of profile and vortex. This means that the quotient length/(2*Strouhal number), the spacing of the vortices, should be at least of the same magnitude as the profile length. The 40 mm cylinder has a Strouhal number of 0.2 and shows a vortex spacing of 40/(2*0.2)=100 mm. Although the aspect ratio of this cylinder is very small, the vortex street is quite stable and has only a single main frequency. Figure 10a shows the frequency at different pressure ratios. The Strouhal number is nearly constant but there is some influence of resonance of the duct geometry.

The 40 mm cylinder and the 120 mm profile were taken for the first vortex-profile interaction tests. Figure 10b shows the arrangement working with an even higher amplitude than the pure cylinder.

For tests with the 60 mm profile several bluff body shapes were investigated (fig. 5). It turned out that a square cylinder has the highest amplitudes and best consistency of Strouhal frequencies over the Reynolds number range. The 20 mm cylinder does not work as well as the bigger one, perhaps because of a different aspect ratio.

4.2. Shock Tube

The shock tube setup uses the same measurement equipment as the duct. The measuring chamber is the same. The length of the tube is 5800 mm. It is sufficient to provide measuring times of 5 ms minimum for the Mach

number range from 0.2 to 0.8. The undisturbed trajectory length of the vortex is at least 400 mm.

Because of the height of the chamber there are restrictions in the attainable length to height ratio of the tube. The length from the membrane to the windows is 2600 mm. Thus the length/height ratio is only 8. As interferograms prove, this small ratio is enough to develop the shock. A problem is the rectangle geometry of the tube. The bursting of the rectangular membrane generates a circular wave. The reflections from the walls are oblique waves. These waves steepen up and form oblique shocks. To prevent these disturbances it was tried to change the bursting process of the membrane by taking other materials and destroying the membrane by high voltage. But this did not work very well and it was found that round shapes of the top and the bottom of the tube prevent uniform reflections of the oblique disturbances.

5. Computer-based interferogram evaluation

5.1. Digitizing and preprocessing

Interferograms are recorded photographically by taking single frames or taking series of interferograms on 16 mm film using high speed pickup techniques. Digitizing of these interferograms is done by an image processing system (IP 512, Imaging Technology), equipped with 2 frame buffers of 512x 512x8 bits capacity each. The image processor is connected to a mini-computer. The system further is equipped with a digitizing tablet and a graphic terminal to enable manual input of graphic data. Also, a computer-controlled film projector is used when consecutive frames of a series of interferograms are to be digitized. A detailed description of the system is given in [15,16]. The digitized TV-lines are fed to the computer and are processed sequentially or stored on disk for subsequent processing. Depending on the quality of the interferograms, different enhancement procedures can be used to increase the signal-to-noise ratio, to correct for uneven illumination or to increase the contrast of the fringes. These preprocessing routines can be done on the image processor, too.

5.2. Fringe segmentation

Fringe segmentation is performed in two steps. First the gray level fringes are converted to binary levels by using a fixed or floating threshold. In the next step the left- und right-edge points of the fringes are collected and stored in a polygonal data structure using a sequential tracking algorithm. To reduce the amount of data to store, a redundancy reduction process approximates the actual polygon by a subset of the vertices of the original polygon within a given range of tolerance.

If fringes leave the field of view, or if a background object resides inside the fringe field (e.g., an airfoil), the visible area of the fringes can be handled by using the points on the boundary as edge points of the fringes. The corresponding polygons of course are not to be along the boundary of the background object, since they may have different fringe orders. In order to establish the boundary test in a quick, easy and robust manner, it is not desirable to derive the boundary information from the fringe field itself. Instead, the geometry of the test section is used to generate a binary-valued mask which is compared with the actual interferogram pixel by pixel while performing the fringe extraction process.

Fringe spacing may be very small at some locations in the fringe fields, as is the case for instance inside the boundary layer, inside a shock wave or near separation lines. If the resolution of the digital system is exceeded at these locations, disconnected or falsely connected fringes may occur. This results in the fact that some of the polygon segments, representing different fringe orders, may be linked together. In order to improve the numbering process, most of the disconnections can be removed by an analysis of some geometrical parameters of the polygons. These geometrical parameters are the shape feature (the circularity defined by the enclosed area divided by the perimeter squared), the ratio of the distance of the polygon endpoints to the length of the polygon line, and the angles between the polygon segments.

Those lines which are suspected to have disconnections are cut by this process at locations where the polygon is folded or where it has sharp edges.

The remaining polygons having disconnections not detected by this cutting process have to be handled by the numbering process.

Some consideration and programming work has been done on the problem of getting numbers for the fringe lines of an interference fringe field by using the known numbers of a similar fringe field. The matter is somewhat more complicated, as some of the lines of the actual fringe field may have disconnections, and therefore it may be impossible to get a unique fringe number for those lines.

The idea of a numbering scheme applicable to series of interferograms is to get additional information from the fringe field numbered previously. This may only be possible when the fringe locations vary only by a small fraction of the fringe spacing at almost any locations of the test section. If the interframe time between consecutive interferograms is choosen appropriately, this condition is satisfied in the case of the profile flow investigation. The numbering of a series of interferograms starts with the setting of the numbers of the first fringe field by hand. The fringe lines are superimposed by a set of so called test-lines at which a set of order number functions is defined by a rational spline approximation. This set of spline functions is fitted to the fringe lines of the following interferogram. The numbers of those fringes overlapping uniquely at the test-lines are accepted directly, the other numbers are derived from the spline functions. An older version of the program uses a set of straight lines running in the x- and y-direction, while a newer version uses a set of polygons as test-lines. The advantage of the polygonal test-lines is that they are more suitably adaptable to the global course of the fringe lines.

In the case where some disconnected lines remain after preprocessing a unique number cannot be assigned to these lines by the numbering scheme. To decide where these lines have to be divided into two or more segments - an older version of the program uses the angles between subsequent polygon segments - the deviations from a local approximation of the fringe order function is used. Another advantage of comparing fringe fields by using local polynomial approximations is the fact that fringe polygons, having no intersections with the test-lines, could be processed using the same algo-

rithm, leading to a more stable behaviour of this numbering process. As the position of the airfoil is not fixed relative to the video coordinates of the scanning equipment (due to imprecise location of successive frames on the film inside the high speed camera and other causes), software had to be developed to achieve automatic adjustment of image coordinates and masking areas. This is especially important when large series of interferograms are to be processed automatically.

5.3. Polynomial approximation

The fringe order function is defined at a set of contour lines, but most of the mathematical transformations to follow require the interpolation of fractional fringe order numbers. Some methods to interpolate between randomly scattered points on a surface are discussed in the literature [17]. We have used a local distance weighted polynomial least squares approximation, best suited in regard to computation time and numerical representation. This process computes the coefficients of two-dimensional polynomials of second order at the mesh points of a rectangular grid. To calculate the interference order inside the meshes, the four polynomials at adjacent corners of the mesh are evaluated and weighted proportionally to their distance to the point of interest.

Another method is to compute a two-dimensional spline approximation, using some of the previously computed polynomial coefficients to get a smooth surface having continuous first and second derivatives. The density function may easily be computed by a linear transformation of the fringe order values, because in the actual experimental set-up the fringes are lines of constant density (infinite fringe case). In the case of finite fringe fields a subtraction of the overlayed fringe pattern could be achieved by a modification of some of the polynomial coefficients.

Routines have been developed to add or subtract the spline approximations describing different fringe fields recorded under equivalent physical conditions. Thus many fields may be averaged and compared with theoretical calculations. This method has been applied to areas where the flow field of interest had been disturbed by turbulence. When the basic flow field chan-

ges slowly as compared with typical time scales of turbulence, and when the photographic frequency is high enough, averaging can be done over consecutive frames to eliminate turbulence. In principle, turbulence could be investigated, too, by comparing single fields with an average (figure 35).

5.4. Localization of the vortex core

In the study of the vortex-profile interaction process a point of interest is the knowledge of the vortex traces under different positions of the profile, to see whether a theoretical description of these traces is in accordance with experimental results. Some program development has been done to localize the typical fringe pattern resulting from the appearance of the vortex. The vortex core is computed using the centroid of the enclosed area of the innermost of these fringe lines.

5.5. Evaluation of interferograms

As an example of digital interferogram analysis two processed fringe fields of a profile flow with and without a vortex present are shown in Figures 11a and 12a. The flow velocities are 280/s and 100 m/s, respectively, at an angle of attack of 0 degrees. The interferograms were digitized with a resolution of 512 by 256 pixels. The fringe extraction process described in chapter 5.2 was used to obtain the polygonal fringe fields shown in Figures 11b and 12b. The boundaries of the test section as well as those of the airfoil are input by hand, using the digitizing tablet. These lines are used to prepare a mask file, needed by the fringe extraction program to avoid connections of fringe lines along the boundaries of background objects. Due to the restricted resolution of the digital system there appeared some falsely connected lines around the leading edge of the airfoil, where the fringe spacing is very small. These locations could be detected and the falsely connected lines could be cut by application of the aforementioned algorithm, using the geometrical parameters of the lines.

The lines are numbered corresponding to the interference order, which in this case is done by hand, because the automatic numbering algorithm, applicable to these types of fringe fields, needs a numbered field to start

the numbering process of consecutive frames. The density function was derived from the fringe field by approximation of polynomials of second order at the mesh points of a rectangular grid (shown in figs. 11b and 12b) as described in chapter 5.2. To achieve a smooth surface, the interference order function was calculated from these polynomials using a bicubic spline interpolation procedure. Two density profiles in x-direction at y = 0.2 are plotted in Figs. 11c and 12c. The relative density as a function of the fringe order is given in this case as

$$\varrho/\varrho_0 = 1 - \frac{1}{n_0(T_E, p_E) - 1} \frac{p_E}{T_E} \frac{T_0}{p_0} \frac{\lambda}{h} \frac{N(x,y)}{2}$$

where o/o is the relative density, n (T, p) is the refractive index of air at temperature T and pressure p, T and p are the temperature and pressure at rest, is the wavelength of light, h the depth of the test chamber and N(x,y) the fringe order function. Note that the order function is divided by two, because each fringe is represented by two lines (a "left" and a "right" one). The above equation, evaluated with the actual dimensions valid in the tests, yields

$$o/o = 1 = 0.01058 * N(x,y)$$

As can be seen from Fig. 17, the lowest density appears inside the vortex core with a value of 0.92 relative to the density at the stagnation point, where the fringe order was set equal to zero.

6. Experimental results of vortex-street-profile interaction

6.1. Pressure fields

Measurements were performed with the 40 mm cylinder with and without the 120 mm profile. The pressure ratio range was from 0.999 to 0.6, that is from 13 m/s to 290 m/s.

As expected, the pressure field is antisymmetric when vortex generator and profile are aligned in the cord plane. The difference from antisymmetry is less than 5 degrees phase angle in Fourier spectra. Therefore it is sufficient to have pressure transducers only in the upper half of the measuring chamber.

Figure 6a shows the pressure transducer positions used in the measurements which are described in this report. Figure 10 is done with pressure transducer 5. Figure 13a and b are typical examples of pressure recordings. At a pressure ratio of 0.83 transducer 2 measures an underpressure of more than 200 mbar. The vortices differ in strength and do not have the same path, so the extreme underpressure peaks only happen from time to time. There is a diffusion of vortex strength and the peaks at transducers 8,10 and 12 do not have such high amplitudes any more. Signals at transducers 5,6,7 and 9 (above profile) do not have single peaks any more but a more sinusoidal shape.

Depending on resonance the peaks of frequency recordings are more or less sharp. But there is always a Strouhal frequency far above the wall turbulence level at nearly all measuring points. Figures 14 to 17 are typical examples of spectra. The spectra are done with 0.8 s long pressure recordings at 10 Khz sample frequency.

At the same pressure ratios vortex street and profile vortex interaction have the same Strouhal frequency. The vortex generation process seems not to be influenced by the profile. The profile measurements show only a slightly better consistancy of Strouhal frequency. The amplitudes in the vicinity of the cylinder are of the same order of magnitude. The amplitudes measured above the profile (transducers 3,5,6,7,9) are greater in the profile case. At any pressure ratio the phase differences between the measuring points are entirely different. The hydrodynamic field as well as the sound field are influenced strongly by the profile.

The first pair of spectra (Fig. 14) is done at the high pressure ratio of 0.998. The velocity is about 19 m/s. Sound generation is inefficient at low velocities. The pressure field is a relatively undisturbed hydrodynamic

field. The Strouhal frequency is of the same magnitude, but the vortex street signals are more noisy. Very obvious is the difference at transducer 1. Only transducer 8 of the profile case shows a noisy character, because it is influenced by the profile wake. It is interesting that the phase differences between the same transducer pairs are entirely different even in the pure hydrodynamic case.

The second pair (fig. 15) has a sharp dominant frequency with the profile and several frequencies with the vortex street, due to beats and frequency jumps. Figure 16 is an opposite example. The vortex street shows the more narrow frequency band, whereas the profile has got a large number of different Strouhal frequencies. Surprisingly, there is the same dominant frequency at all measuring points.

Figure 17 is a resonance case with extremly high amplitudes. There is the same frequency at all measuring points and nearly the same frequency in both plots. (The first harmonic has a higher amplitude at transducer 1 and 8, but the fundamental is the same). In both cases the highest amplitudes are at transducers 2 and 3. The transducers above the profile (3,5,6,7,9) have higher amplitudes with the profile. The greatest difference is in the first harmonic (fig. 18). There is a harmonic at transducers 1,2,3 in both cases, but the profile shows higher amplitudes and higher quality factor. Entirely different are the transducer signals above the profile (5,6,7,9) where the vortex street shows noise and the profile shows the first harmonic with high amplitudes and high quality factor. This might be a hint that a new phenomenon is occurring with strong vortices at high Reynolds numbers.

6.2. Phenomena of interaction

The boundary layer plays an important role in vortex airfoil interaction. The closer the vortex gets to the airfoil, the stronger is the effect on the boundary layer. Figure 19 is an overview on the different interaction phenomena. (The flow comes from the left side, the sense of direction of the vortex is counterclockwise). The interaction is shown in 4 time steps. Depending on the distance to the airfoil axis, we can find eight (a-h) principally different cases. The phenomena are very much alike for Mach

numbers from 0.2 to 0.8 and circulation coefficients from 0.3 to 1.5. The case f happens only at circulation coefficients above 0.2. Case c needs a circulation coefficient above 0.5 or a high Mach number.

Cases a and h: There is nearly no interaction with the airfoil boundary layer at a greater distance from the airfoil axis, that is more than one third of airfoil length at a circulation coefficient of 0.5. Only the stagnation point is moving downwards and a tiny suction region is generated on the upper side of the airfoil. After the vortex has passed the leading edge there are no strong deviations from the stationary flow around the airfoil.

Cases b and g: When the vortex comes closer to the airfoil the interferogram shows a small thickening in boundary layer between vortex and airfoil boundary. The thickening is generated at about one quarter of airfoil cord-length. It is travelling with the vortex and it is slowly growing. This thickening can be the source of a secondary vortex when the interaction is strong enough. This secondary vortex is generated downstream of the primary vortex if the vortex is above the airfoil and upstream if the vortex is below the airfoil.

Cases c and f: If the vortex is stronger there is a separation in the suction peak which becomes a secondary vortex. Case f, where the vortex passes under the airfoil occurs only at circulation coefficients above 2.0. At very high circulation coefficients of about 4.0 there is separation at the suction peak if the vortex is still more than half an airfoil length away from the leading edge.

Cases d and e: If the vortex hits the leading edge directly, it vanishes totally (Case e). If the vortex passes very close to the profile the vortex looses a lot of its circulation and only a very small turbulent spot is left (Case d).

The figures 20,21,22 and 23 are examples for the cases b, c, e and f. The Figures 20,21 and 22 are related to the shock tube experiment while fig. 12 comes from the stationary wind tunnel experiment. Figure 20 contains ten frames. A vortex is coming from the left side and, while passing the air-

foil, it generates a secondary vortex. Figure 21 and 22 are experiments at the high Mach number of 0.8. In the first of the 5 frames the shock wave and the vortex are at a close distance. Before the vortex gets into contact with the airfoil it passes the leading edge reflection of the shock. When the vortex gets close to the leading edge there is a strong interaction. In both cases the vortex nearly vanishes. But this strong interaction generates a strong acoustic wave. Figure 23 shows an interaction of the airfoil with a vortex of the high circulation coefficient of 4. There appears a strong secondary vortex generated in the suction region of the airfoil.

6.3. Experimentally determined vortex paths

According to theoretical calculations as described above and by other authors [2,11,6] the generation of sound depends on the path of the vortex. Therefore, precise knowledge of these paths is necessary for testing these theories. Figures 24,25,26 show paths of vortices under different conditions in comparison with streamlines of incompressible flow around a Joukowsky profile. Short streamlines near the trailing edge indicate secondary vortices.

Far away upstream the vortices move uniformly with the flow. Near the leading edge they deviate from the streamlines in an upward direction. This deviation is larger at small Mach numbers then at large ones. This agrees with a prediction by Lindblad [18].

The behaviour of the vortex after passing the leading edge depends on the distance from the profile. If the vortex hits the leading edge precisely, it disappears. When the distance is small, a strong interaction with the boundary layer takes place and secondary vortices are generated. This reinforces the upward movement of the vortex above the upper face of the profile; this movement continues after the vortex has passed the trailing edge. (An exception to this is the case $M = 0.4$, $Z = 2.0$, where the secondary vortex is stronger than the residue of the primary one, which does rotate around the former).

The appearance of a secondary vortex enlarges the distance between vortex and profile under the lower face, too.

With increasing distance from the profile secondary vortices are not generated any more. The vortex reaches its uppermost point approximately above the centre of the profile. Then it moves downwards as compared with the streamlines. The path of the vortex is approximately symmetrical with respect to the mid-perpendicular of the profile.

The vortex paths calculated with the model described above are in qualitative agreement with the theoretical results when the vortex-airfoil separation is large. However, a quantitative comparison shows grave disagreement. The first and third plot of figure 27 show a close contiguity of theoretical and experimental paths, but only because both don't deviate from the streamlines very much.

Figure 28 shows an example of large deviation from the streamlines. As is the case in the other examples, the theoretical values are nearer to the streamlines than the experimental ones. The second plot in Figure 27 shows a comparison between experimental data and theoretical results calculated without taking into account a central vortex of circulation. (In this case the circulation around the profile doesn't equal zero but the negative value of the circulation of the vortex.)

Calculated deviations of the vortex path from the streamlines are larger than in the model with a central vortex and larger than the experimental values, too. Reality seems to lie somewhere between these two possibilities. Circulation around the airfoil apparently changes when a vortex is passing. Therefore, no reasonable agreement can be achieved when the model described above is used.

It can be concluded that simple models of potential theory describing the passage of a vortex near an airfoil will meet basic difficulties. To achieve a better understanding, precise knowledge of the influence of the boundary layer will be necessary. A further difficulty is that the mechanism of varying circulation of the airfoil is not yet understood.

6.4. Generation of sound

Theory predicts the generation of sound with wavelength of the order of

magnitude velocity of sound (time of passage) when the height of the vortex above the horizontal axis of the airfoil exceeds 0.1. The wavelength then is larger than the profile, which is an assumption of this theory [1,2]. As the paths of the vortices are not predicted accurately, one cannot hope for quantitatively correct results. However, some qualitative agreement can be expected.

Waves of such a low frequency cannot be detected in interferograms, but earlier meassurements indicated the appearance of low frequency sound [19].

In addition to low frequency sound, sound waves of very short wavelength are generated. Shocks appear at higher Mach numbers (0.6, 0.8; 0.4 in some special cases) these shocks emanate from the leading edge of the profile. As the flow near the leading edge does not depend strongly on the flow at other parts of the airfoil, the wavelength of this sound presumably depends on the radius of curvature of the leading edge and the core radius of the vortex.

Figure 29 shows 4 series of interferograms recorded under equal conditions. The vortex directly hits the leading edge. The first picture of every series shows the shock wave and its reflection off the leading edge. The interaction of the vortex with the reflected cylindrial wave is apparent in the second picture of the first series. As a consequence of this interaction, a secondary wave behind the reflected shock appears in the consecutive pictures which is inclined to the right by approximately 10 - 15 degrees as compared with the reflected shock. The second pictures of the three other series show the vortex core immediately before hitting the leading edge. The vortex disappears almost completely; only weak residues can be discerned (3. picture of 2. and 3. series). Instead, a strong cylindrical wave has appeared, the centre of which is located near the leading edge. This wave steepens to form a shock wave (4. and 5. picture).

A binary structure is characteristic for the generated wave (3. picture, 4. series). The length of the wave is comparable to the width of the high velocity region immediately behind the leading edge (2. pictures). This region vanishes too fast for the process to be resolved with a photographic frequency of 10 kHz.

The stagnation point jumps to the front which results in a pressure jump at the leading edge. The increase of pressure at the upper face is much stronger than the decrease at the lower one, so a monopole-like emission is likely. The region of increasing pressure extends from the leading edge to approximately 1/4 of the chordlength. The thickness of this region - and therefore a characteristic length of the wavelength of generated sound - is smaller than its extension in the direction of flow. Therefore, emission must take place in the normal direction. Figure 30 shows 4 consecutive stages of propagation of the generated wave.

If one approximates the wave by a cylindrical one, the centre of the cylinder is located near the lower face and moves to the right with the velocity of the flow. An angular characteristic has been plotted for the circle with its centre indicated by a cross. The outer circle corresponds to a density difference of one fringe, approximately are third of the stagnation density. The maximum of the lobe is at appr. 45 degrees in the upper left. The maximal amplitude is at appr. 0.7 fringes, corresponding to 0.2 times the stagnation pressure. As the infinite fringe mode of measurement has been used, only a few fringes appear. Therefore, experimental uncertainties are quite large. The maximum amplitudes of the four waves differ by about 50 %. The form of interaction depends sensitively on the height of the vortex above the horizontal axis of the airfoil in the case of direct hits.

The location of the centre of the wave under the airfoil indicates that the wave is emitted off an extended region, so the centre appears to be situated behind the actual region of generation.

When the vortex does not hit the leading edge directly, more complicated processes take place. The vortex does not disappear but interacts with the low pressure region of the airfoil. Pressure increases at the upper face in this case, too, but the region of maximal pressure change cannot be located as precisely as in the case of a direct hit.

Two cases of a vortex passing above the profile are shown in Fig. 31. The vortex passes far away from the airfoil axis in the series at the left. An interaction of type c) takes place. A low pressure region to the right

of the vortex can be discerned on picture 2. A secondary vortex and a compression wave become apparent (picture 3). The other series is more similar to the first case. Although the vortex does not disappear completely, the disappearance of the low pressure region is analogous to the case of a direct hit. The wedge of low pressure downstream above the vortex which appears in conjunction with vortex generation can be seen in Figure 31 and should not be confused with a sound wave.

Figs. 32a and 32b show a cross section of the pressure and an angular characteristic. The waves are circular in both cases, their center lying a bit beneath the centre of the airfoil.

The amplitude is smaller than that of the wave in 32b by a factor of about 2, their radii being about equal. The angular characteristic is similar in both cases. Because of the stronger circulation of the vortex, the amplitude is larger in case 32b than in that of 30. As the radius of the wave is larger than in 30, too, the relation between circulation and amplitude appears to be approximately quadratic.

Figs. 21,22 show a comparison between a vortex passing over and under the airfoil, respectively. Angular characteristics are shown in Fig. 33.

The density on the upper face of the airfoil has been plotted for 7 points in Fig. 34. Pressure decreases when the vortex is approaching (example at the left); there is a steep increase of pressure after the passage of the vortex. As has been explained above, these pressure changes cause the generation of sound. However, the temporal resolution of the measuring equipment is not yet sufficient to resolve the process of generation in sufficient detail.

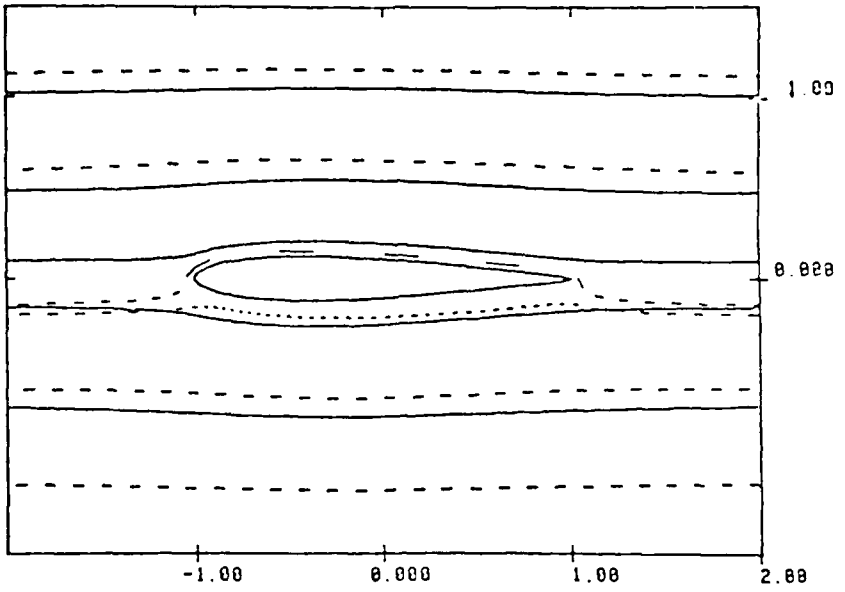

figure 1a: 6 vortex trajectories around a Joukouwsky airfoil (dashed lines), the circulation coefficient is 1. The solid lines are streamlines of stationary flow.
(sense of direction of the vortex is counterclockwise)

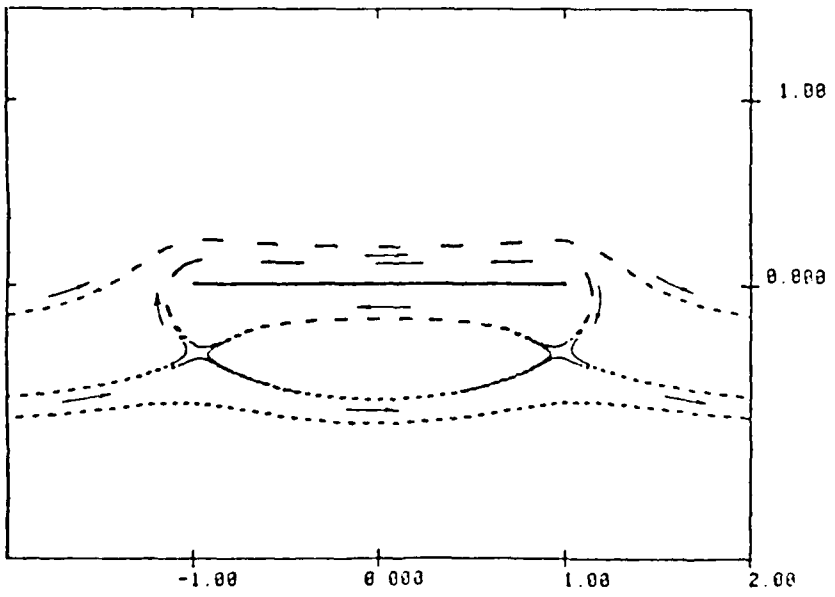

figure 1b: 6 vortex trajectories around a flat plate, the circulation coefficient is 10. The flow is from left to right, the sense of direction of the vortex is counterclockwise.

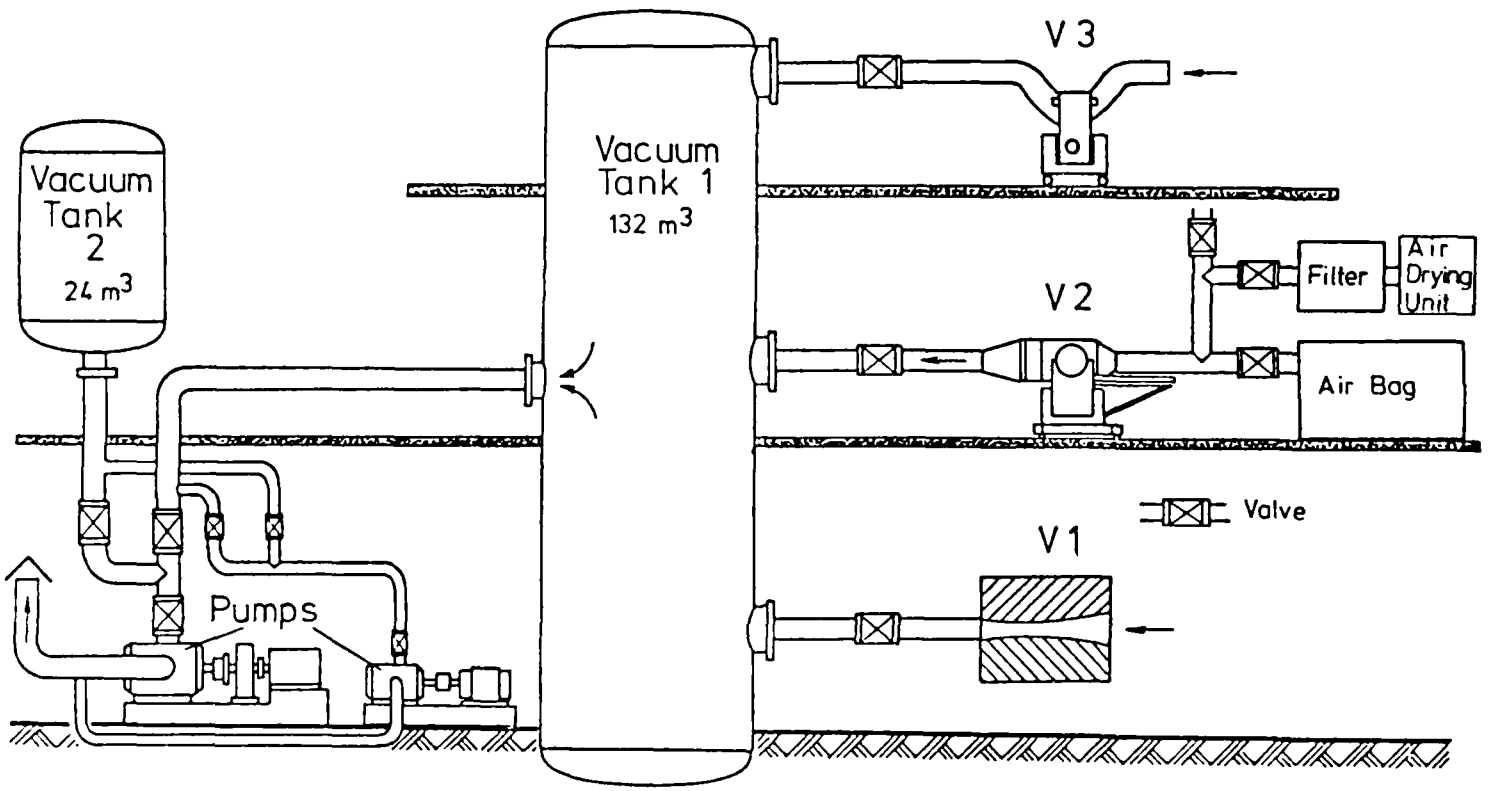

Figure 2 : The transonic duct. Experiments are carried out at facility V2.

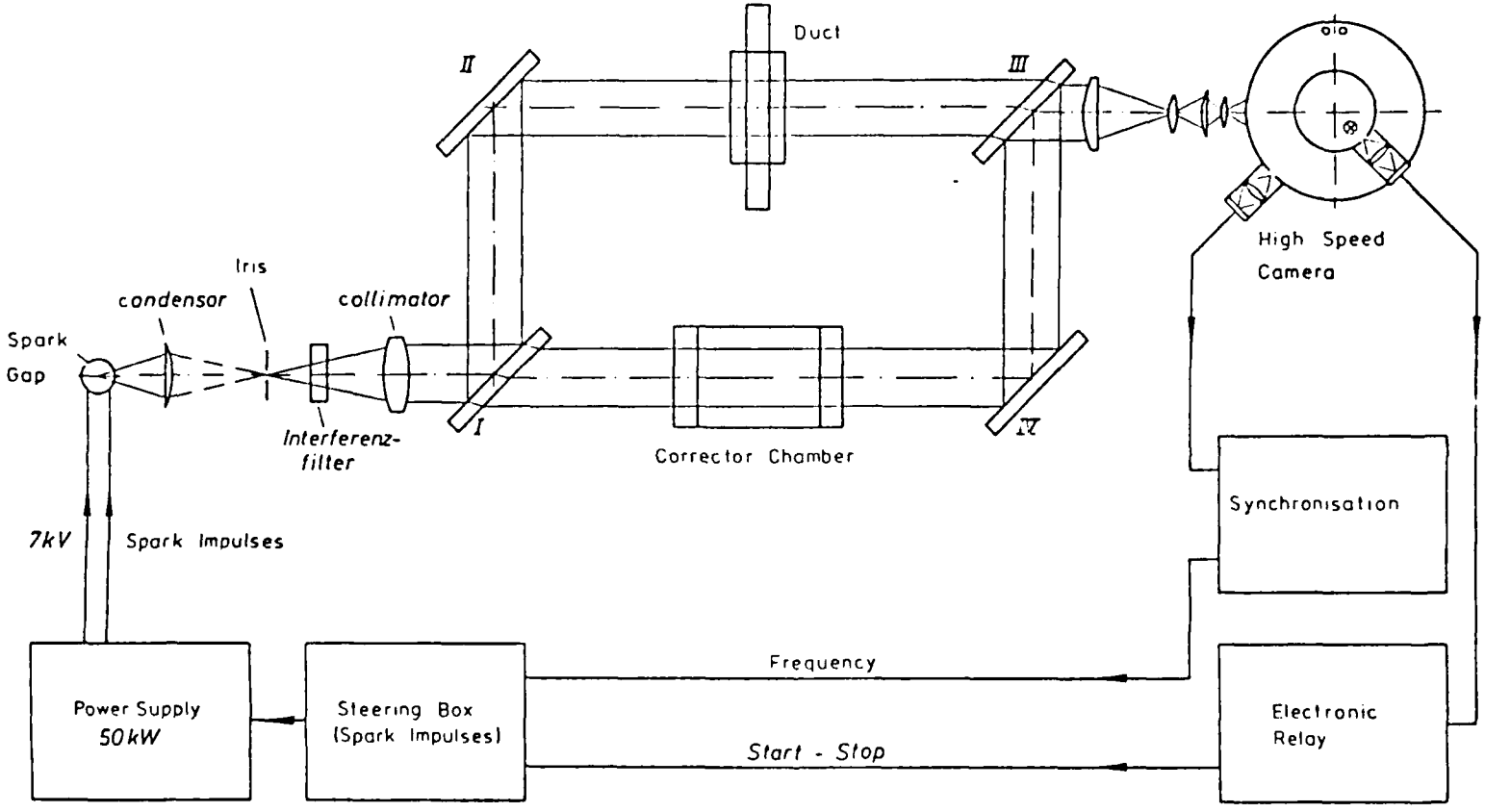

Figure 3: Optical facility for high speed interferogram movies.

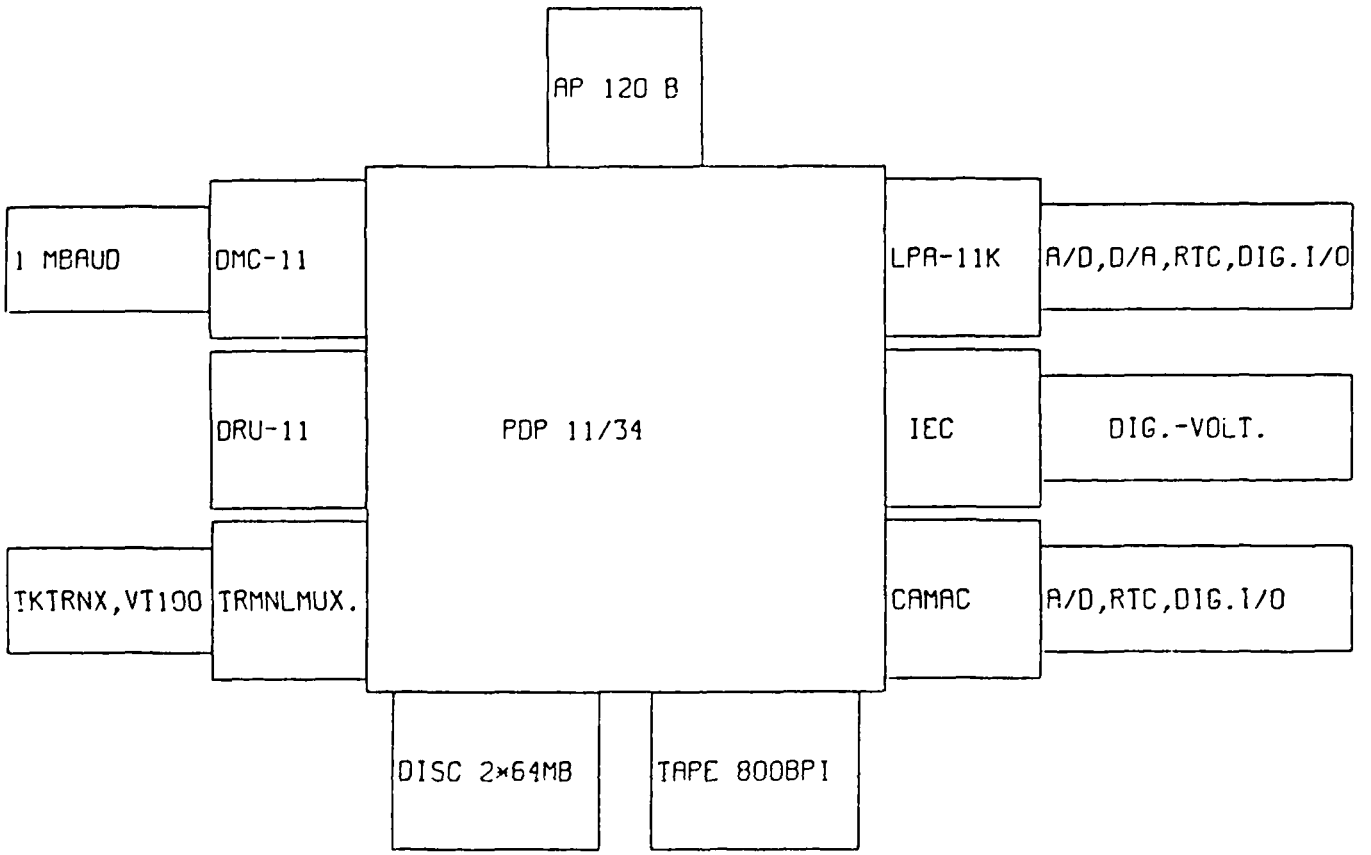

Figure 4 : Computer installation.

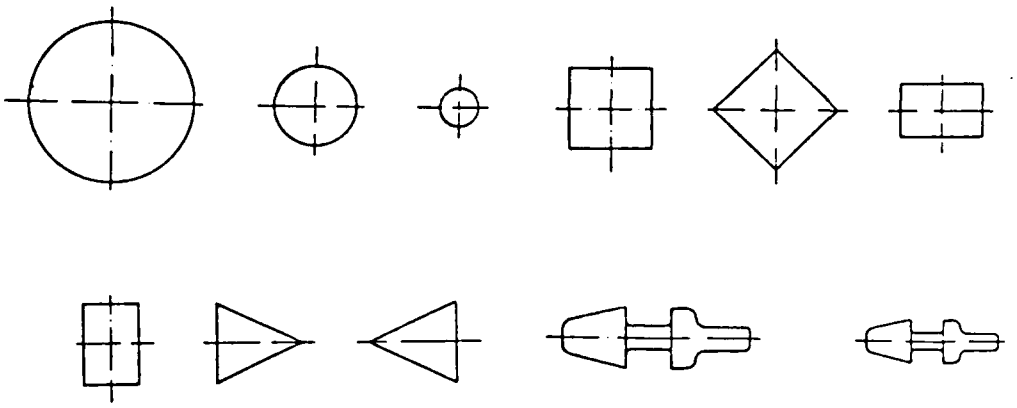

Figure 5 : Bluff body vortex generators:
Circular cylinders of 40, 20 and 10 mm diameter, square, rectangle and triangle cylinders of 20 mm width and a special shape, that is used in vortex flow meters.

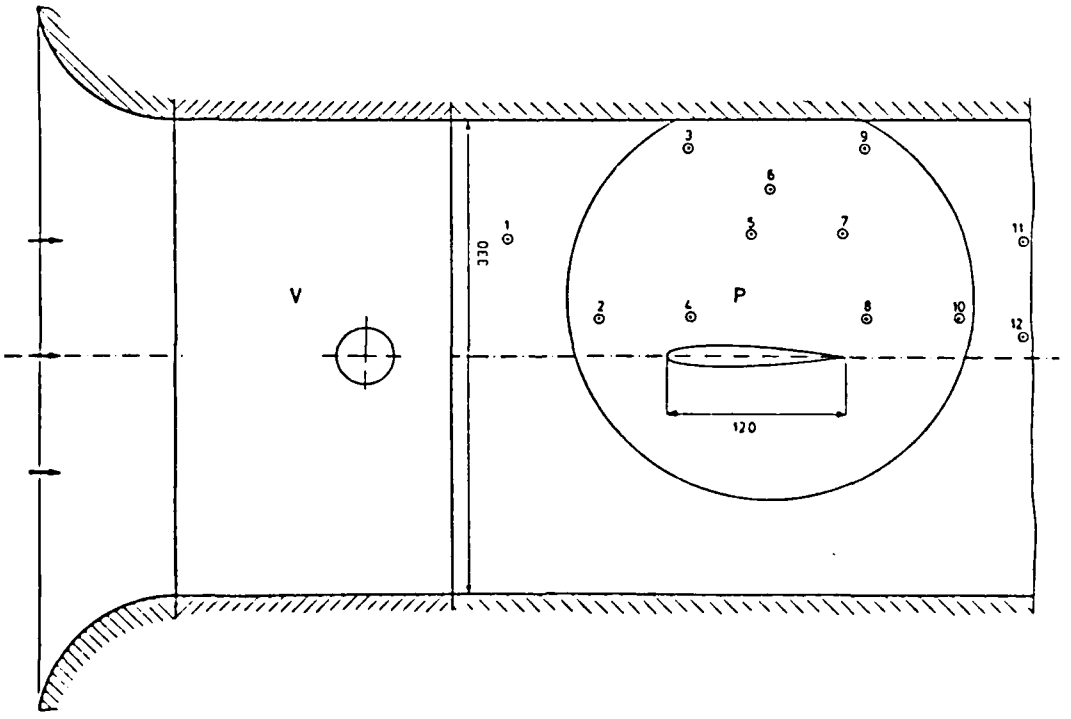

Figure 6a : Measuring chamber for vortex street - profile experiments. Points 1 - 12 are transducer positions.

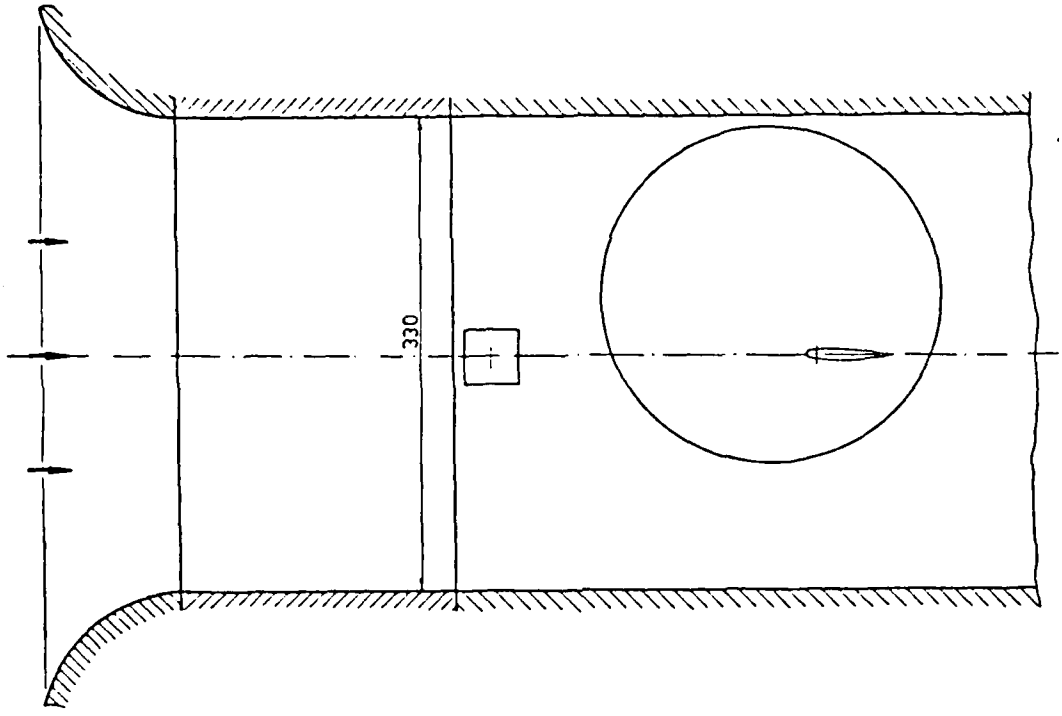

Figure 6b: Experimental setup for figure 18 (without profile) and figure 19 (with profile). 40 mm vortex generator and 60 mm profile.

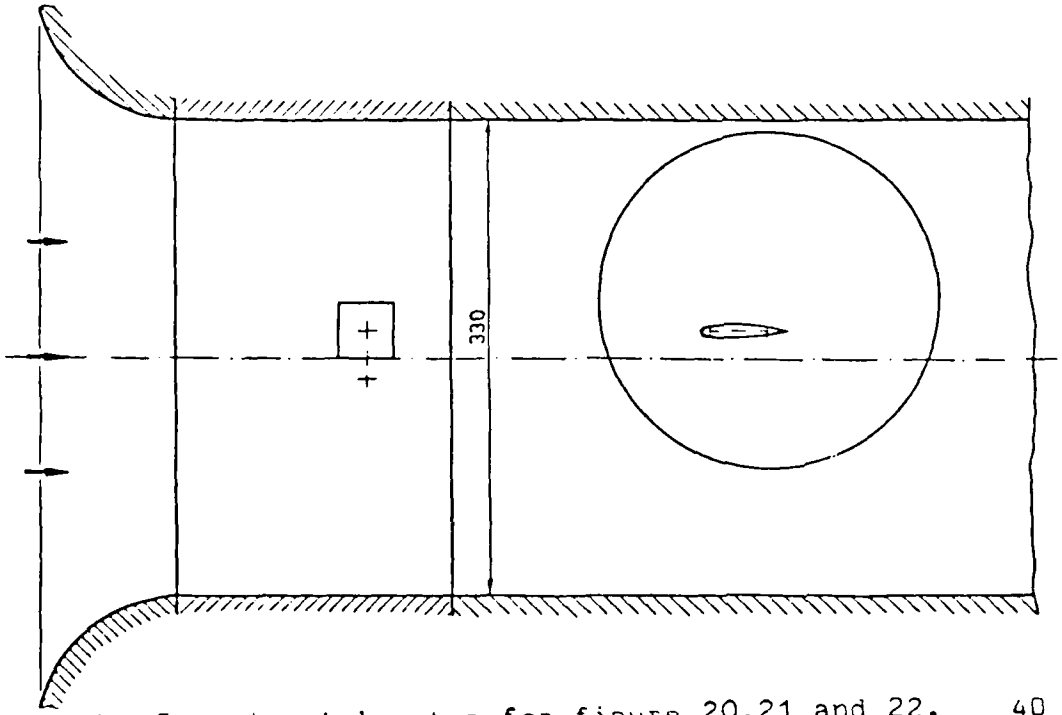

Figure 6c: Experimental setup for figure 20,21 and 22. 40 mm vortex generator and 60 mm profile. The vortex generator is mounted in line with the profile (20), 20 mm and 35 mm under the profile (21,22) .

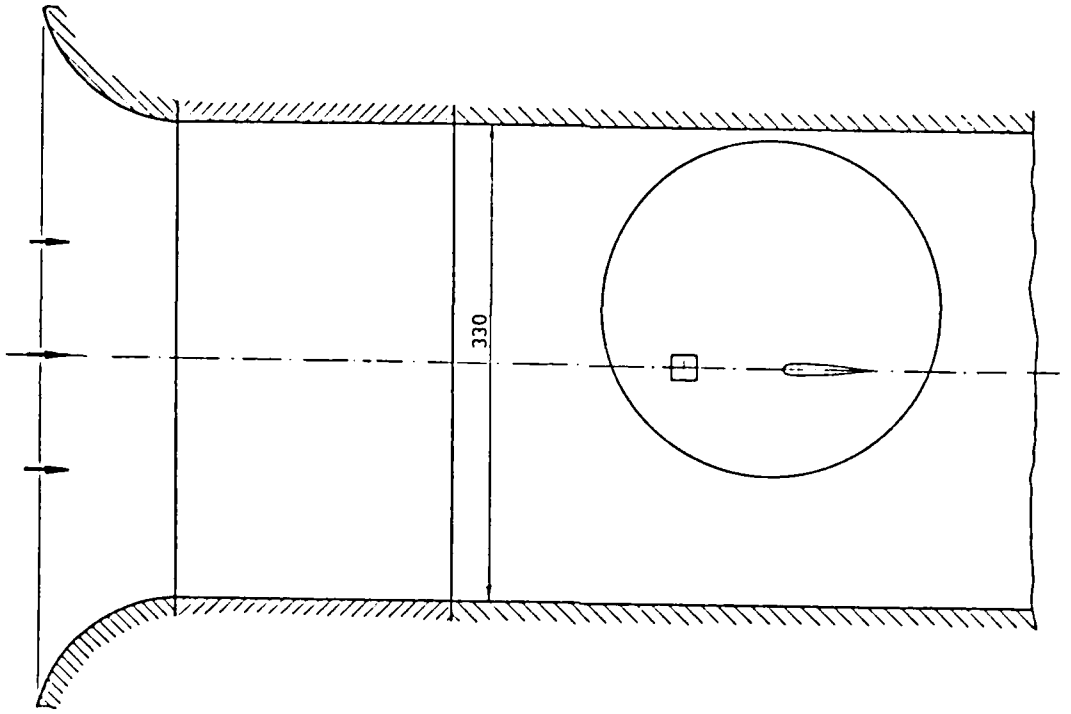

Figure 6d: Experimental setup for figure 23 . 20 mm vortex generator and 60 mm profile are mounted in line in the window area.

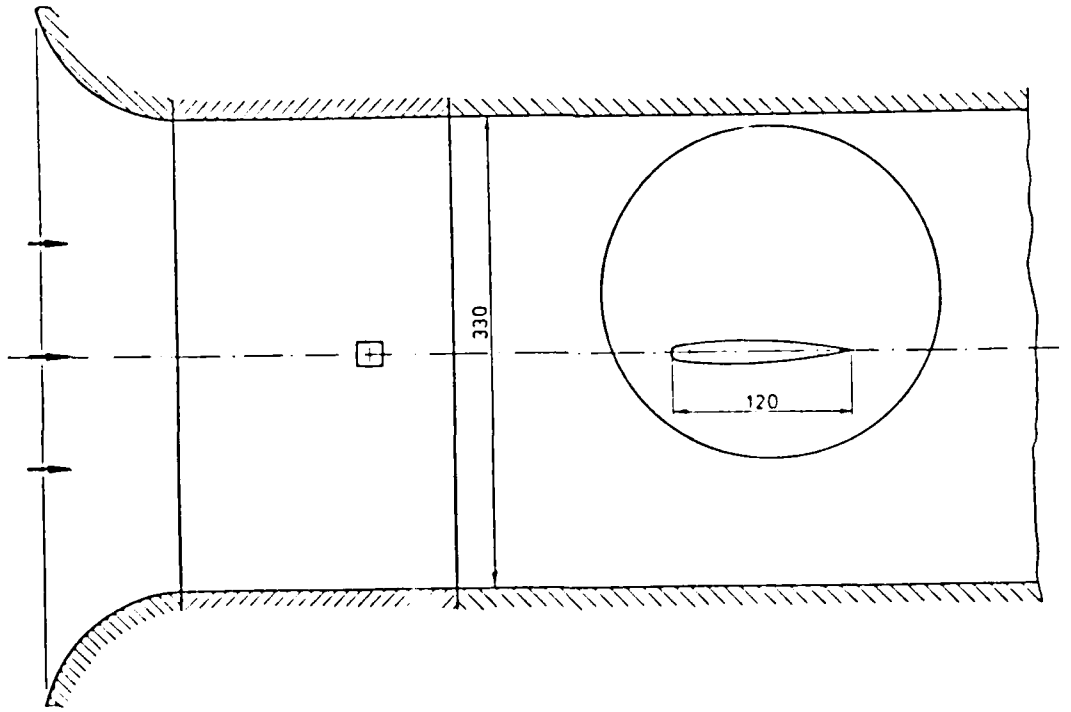

Figure 6e: Experimental setup for figure 24 . 20 mm vortex generator and 120 mm profile.

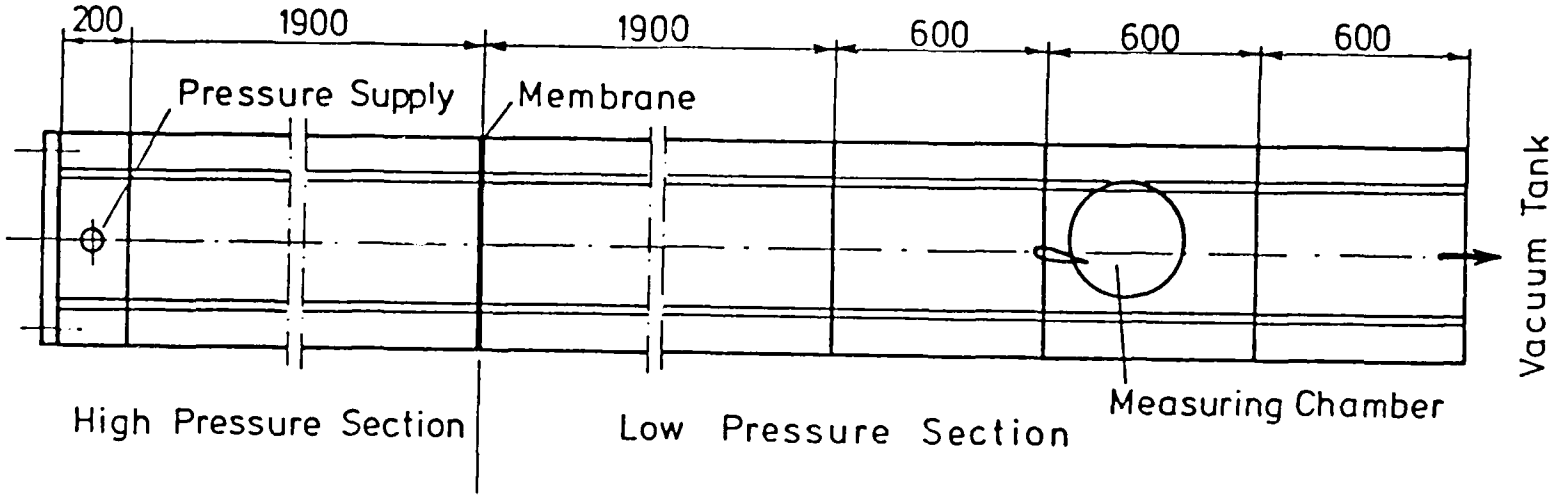

Figure 7: Side view of the shock tube.

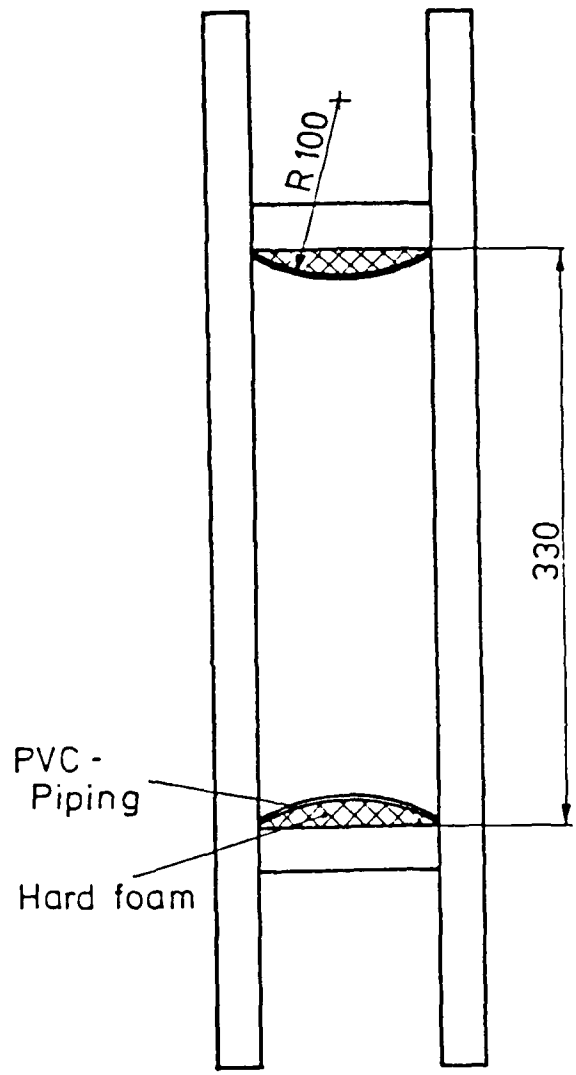

Figure 8 : Front view of the shock tube. The bottom and the top of the tube are round to prevent shock disturbances.

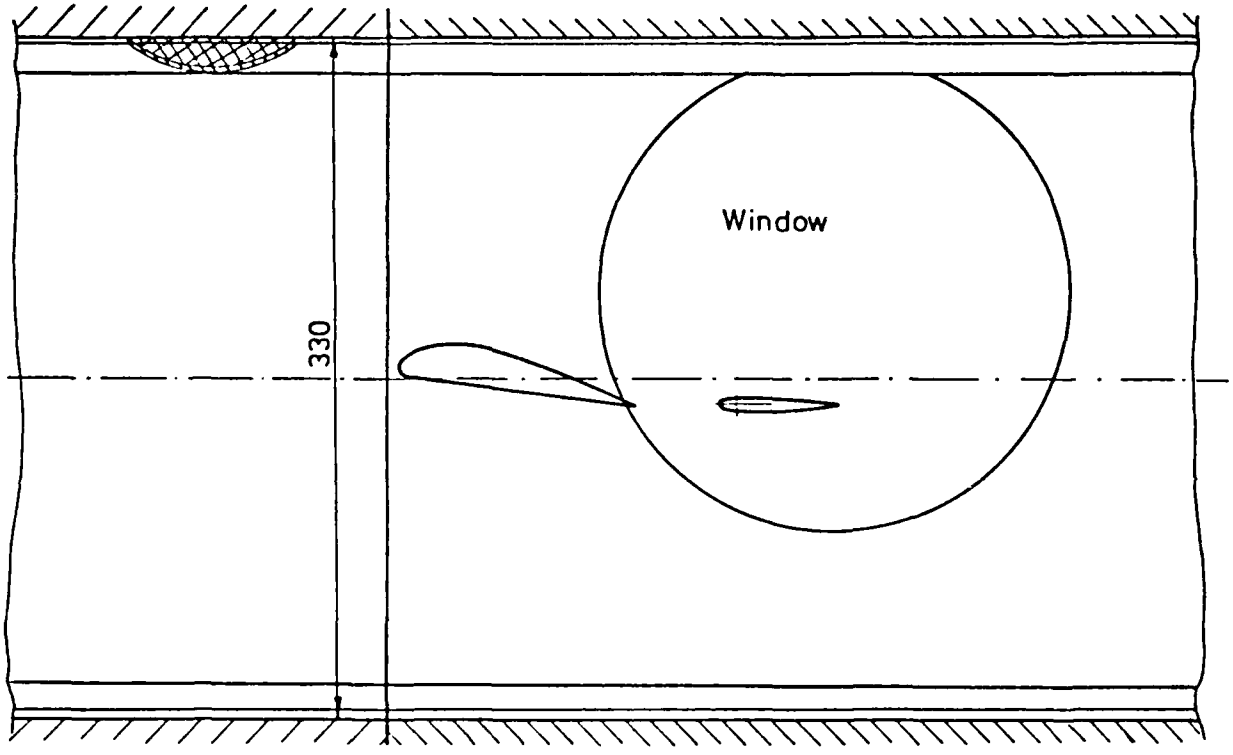

Figure 9: Measuring chamber of the shock tube. A 120 mm GOE 508 profile is mounted at an angle of 7.5 degree. A 60 mm NACA 0012 is mounted in line with the trailing edge.

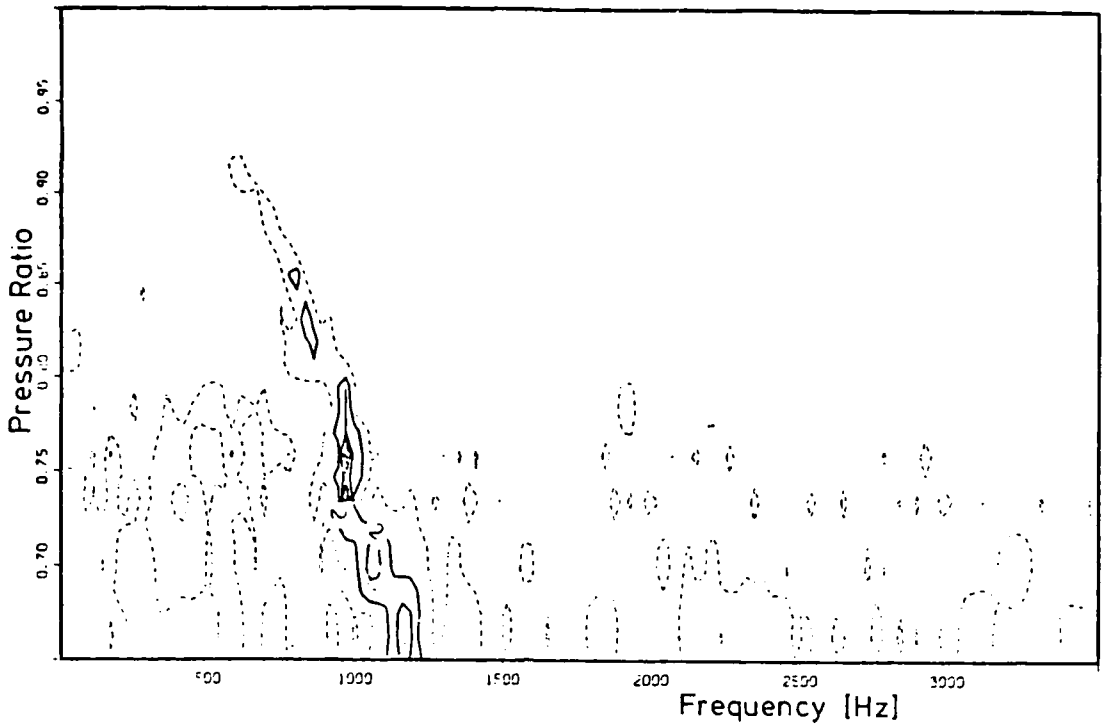

Figure 10: Fourier spectra at different pressure ratios.

10a: Vortex street
Transducer 5 Maximal Amplitude: 14.17 [mbar]

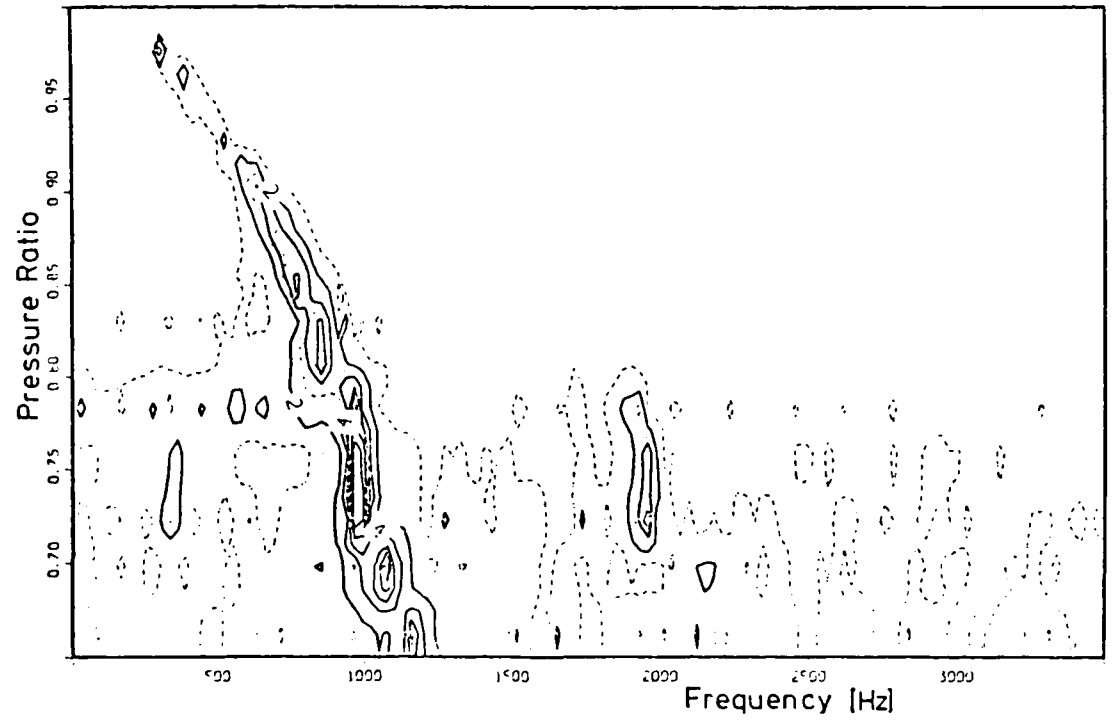

10b: Profile - Vortex Street Interaction
Transducer 5 Maximal Amplitude: 49.92 [mbar]

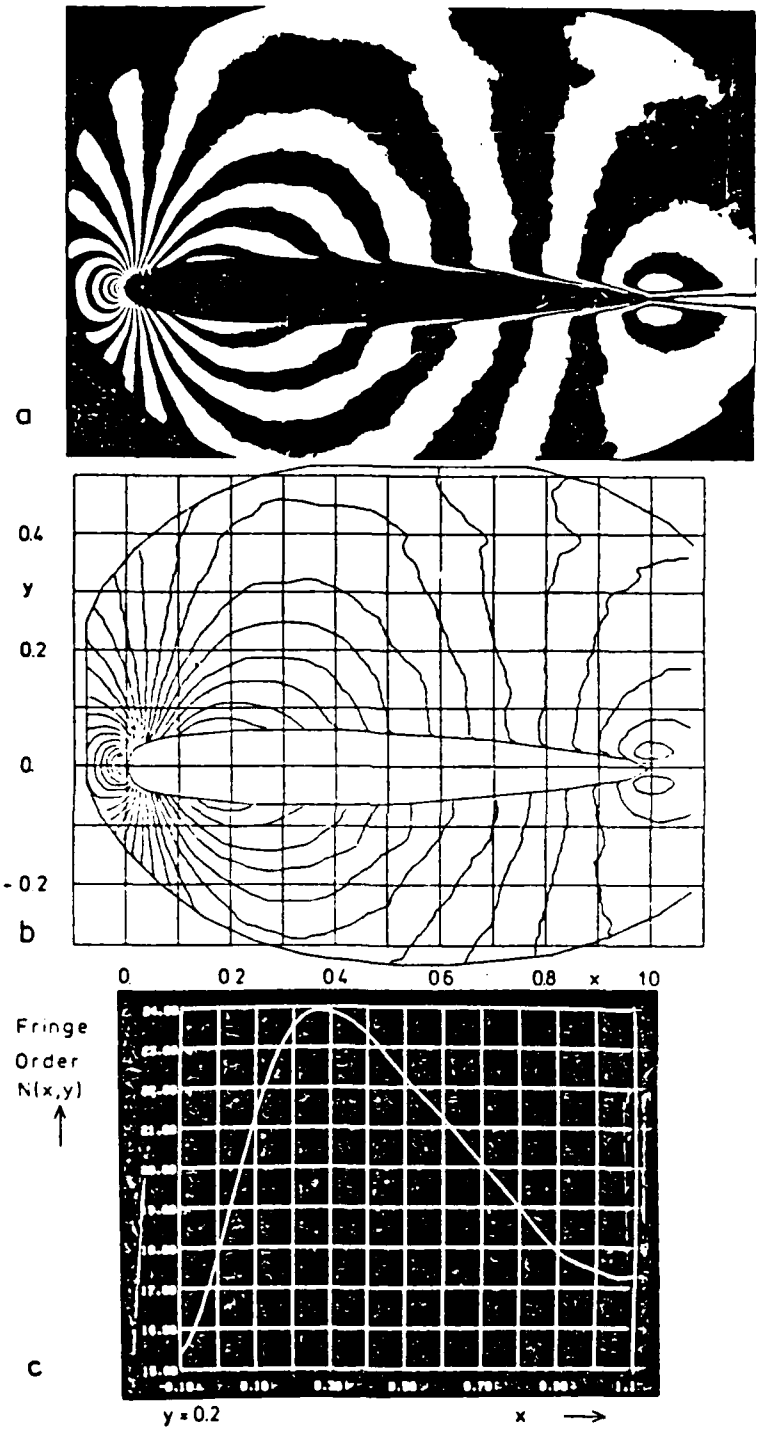

Figure 11 : Example of evaluated interferograms

a) Photo of a profile flow interferogram

b) Plot of the segmented fringes of Fig. 11 a after removal of the line disconnections. The mesh lines used for computing of the polynomial coefficients as well as the boundary lines of the testsection are included for illustration.

c) Density profiles plotted from the spline surface of the order number function of Fig. 11 b along the x-direction at y=-0.2 The density is given in relative units (fringe numbers); high values represent low densities.

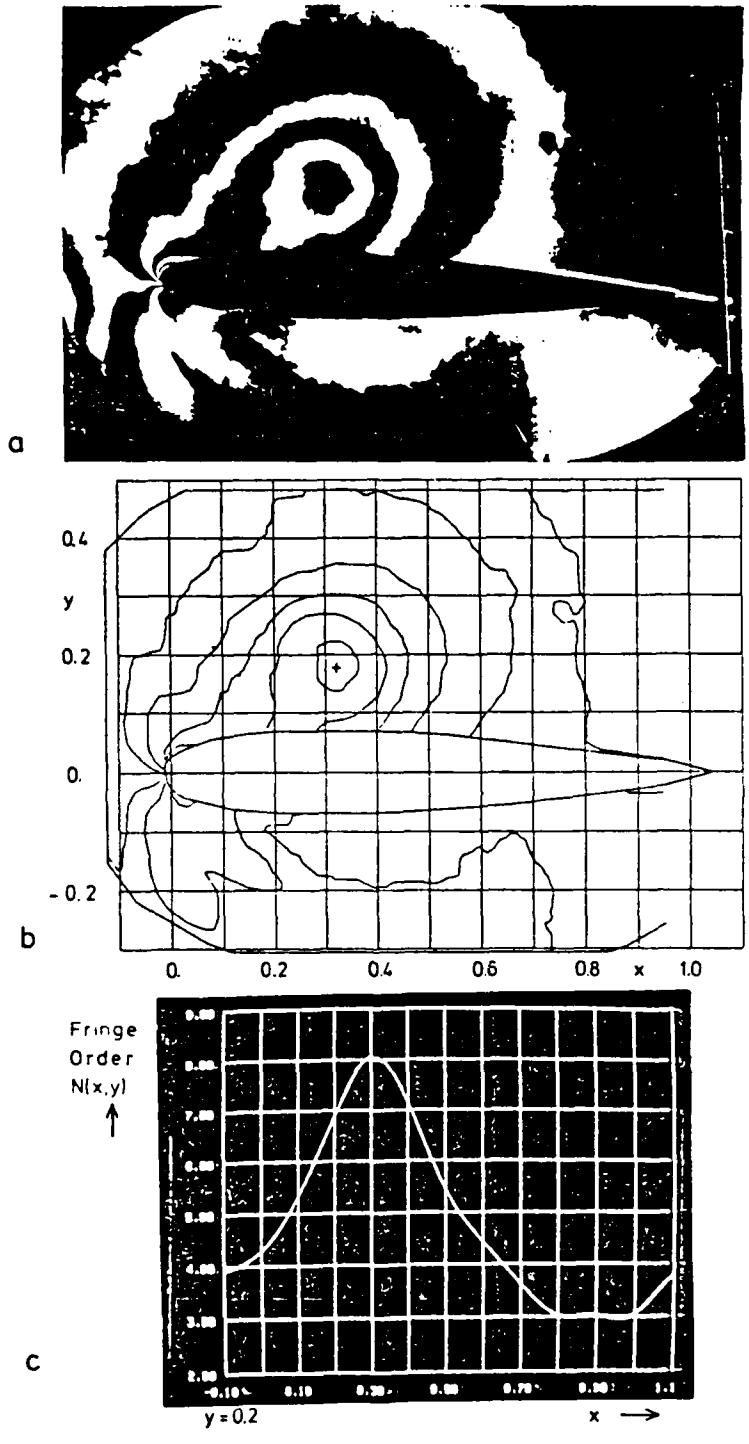

Figure 12: Example of evaluated interferograms
a) Photo of a profile flow interferogram with vortex
b) Plot of the segmented fringes of Fig. 12a after removal of the line disconnections. The position of the vortex core is at (x,y)=(0.32,0.18).
c) Density profiles plotted from the spline surface of the order number function of Fig. 12b along the x-direction at y=-0.2 The density is given in relative units (fringe numbers); high values represent low densities.

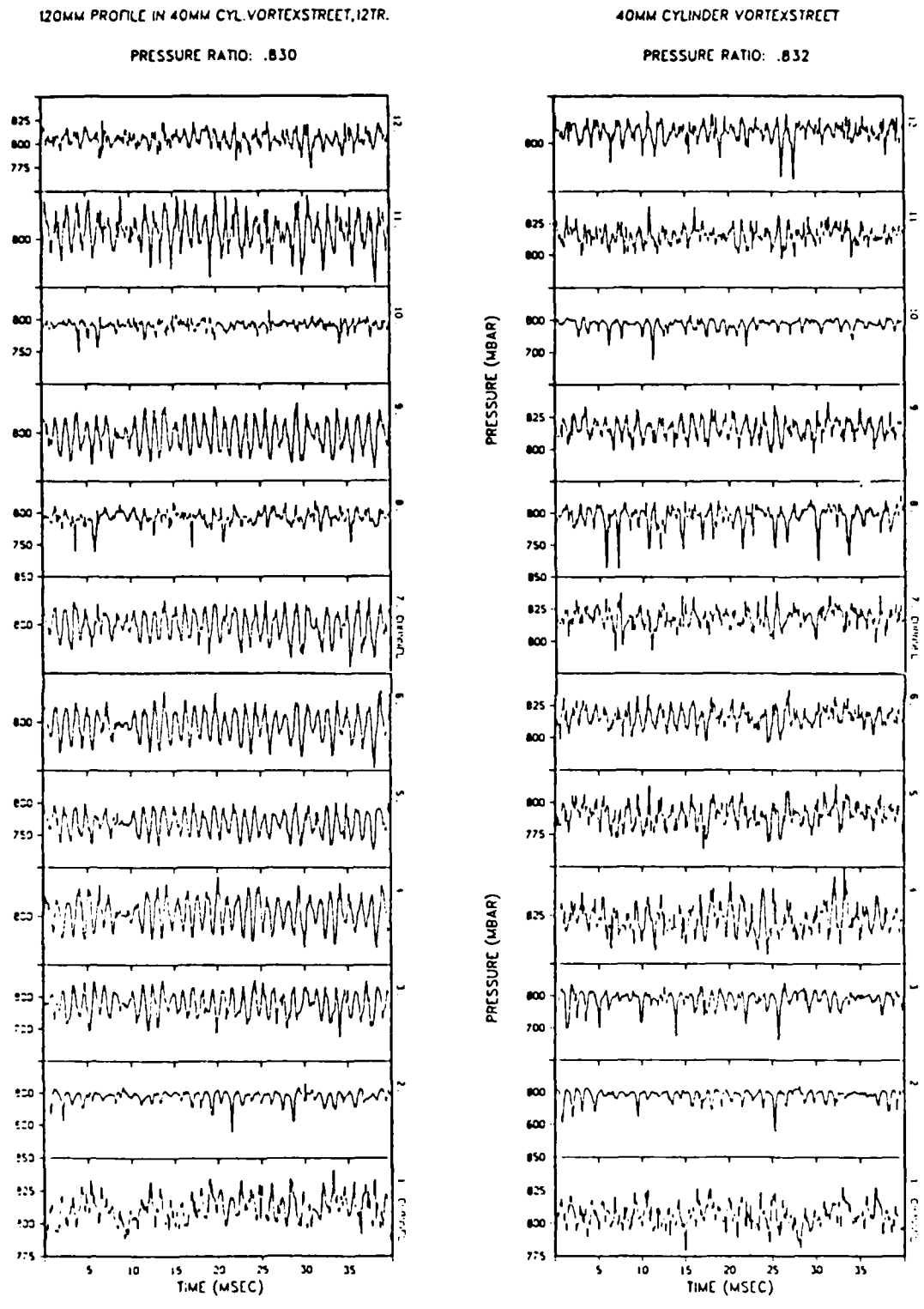

Figure 13 a and 13 b

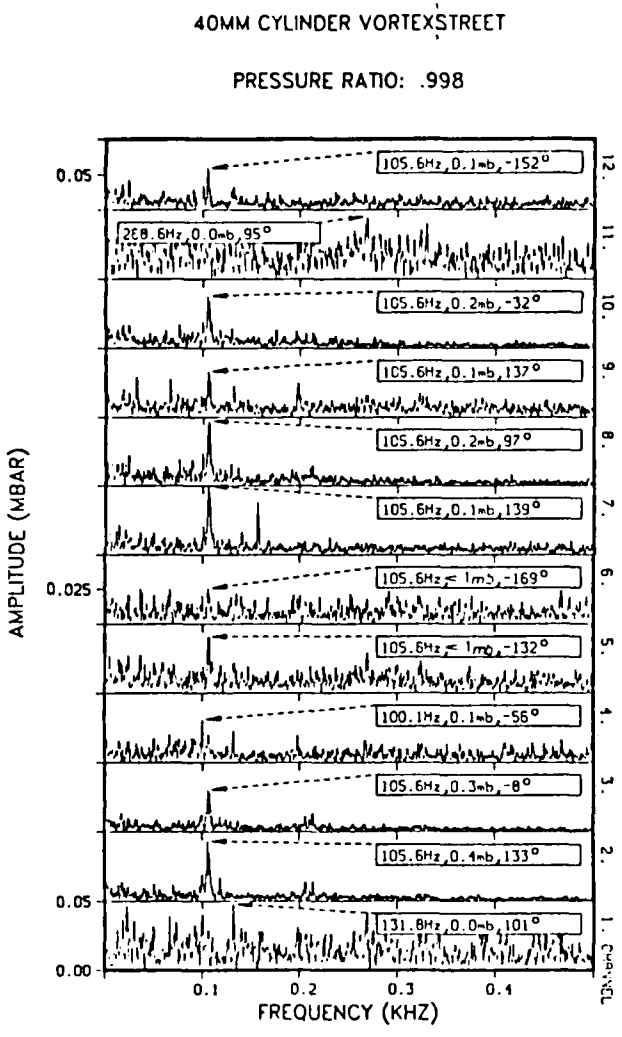

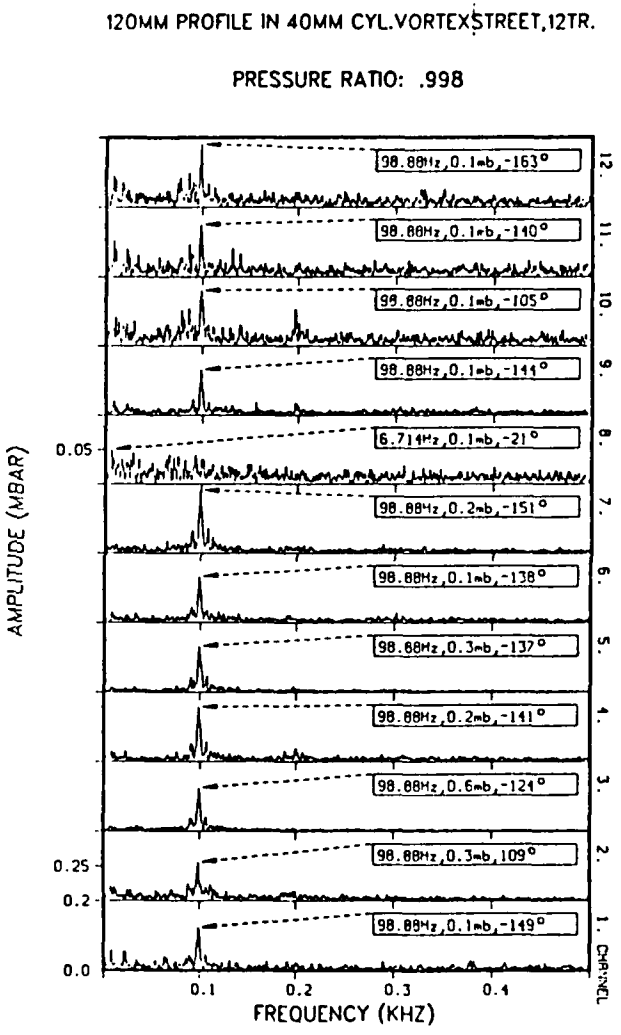

Figure 14a and 14b

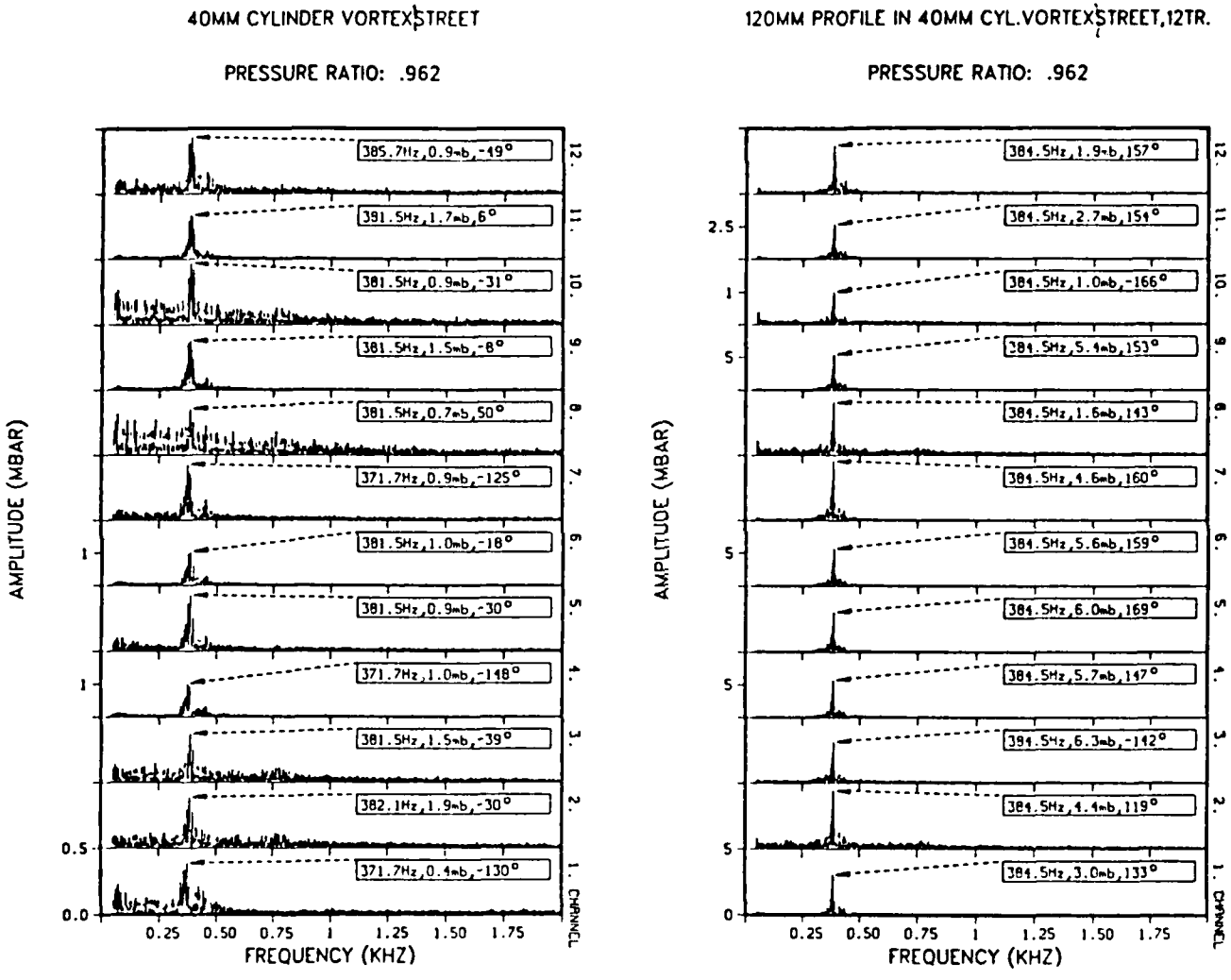

Figure 15a and 15b

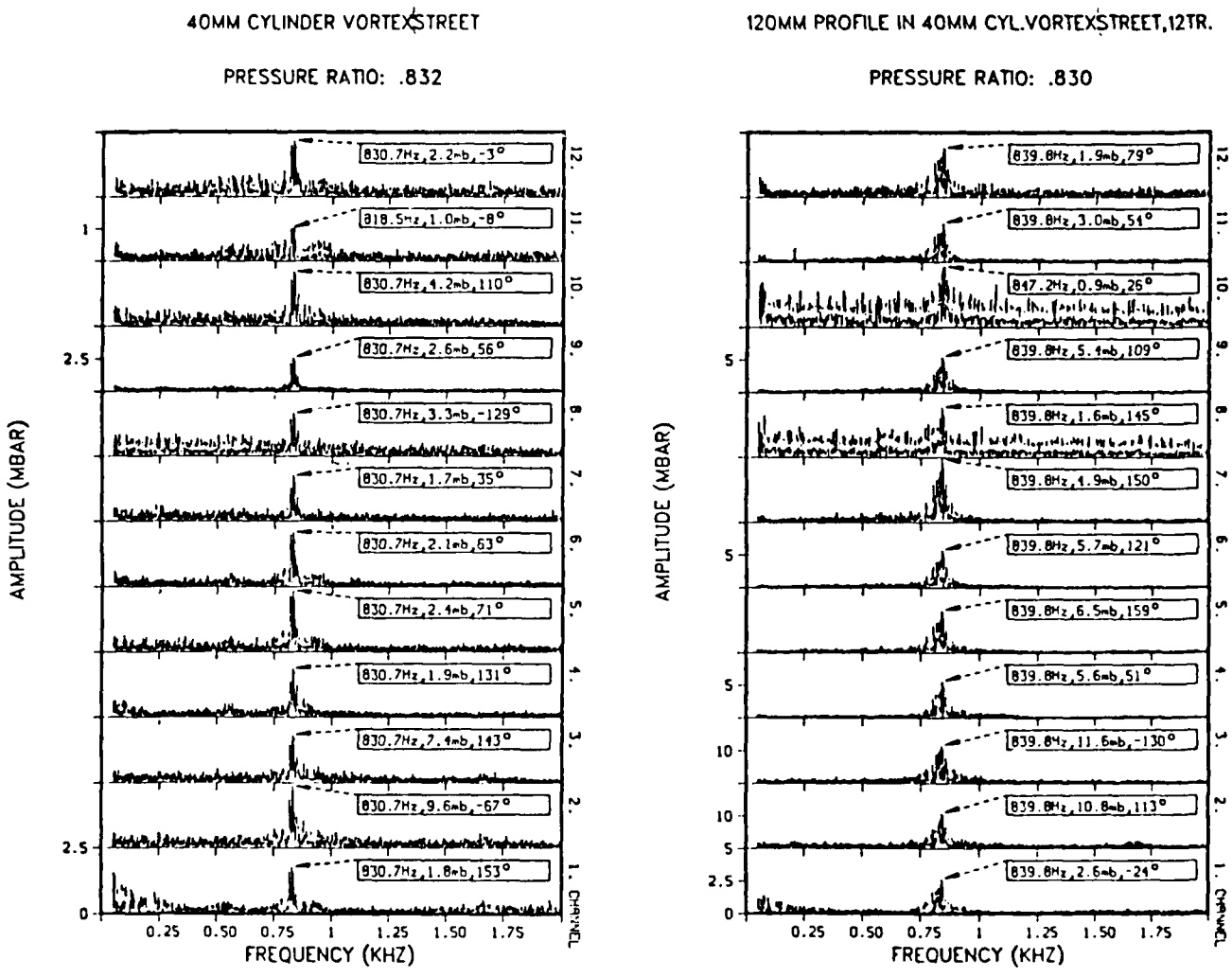

Figure 16a and 16b

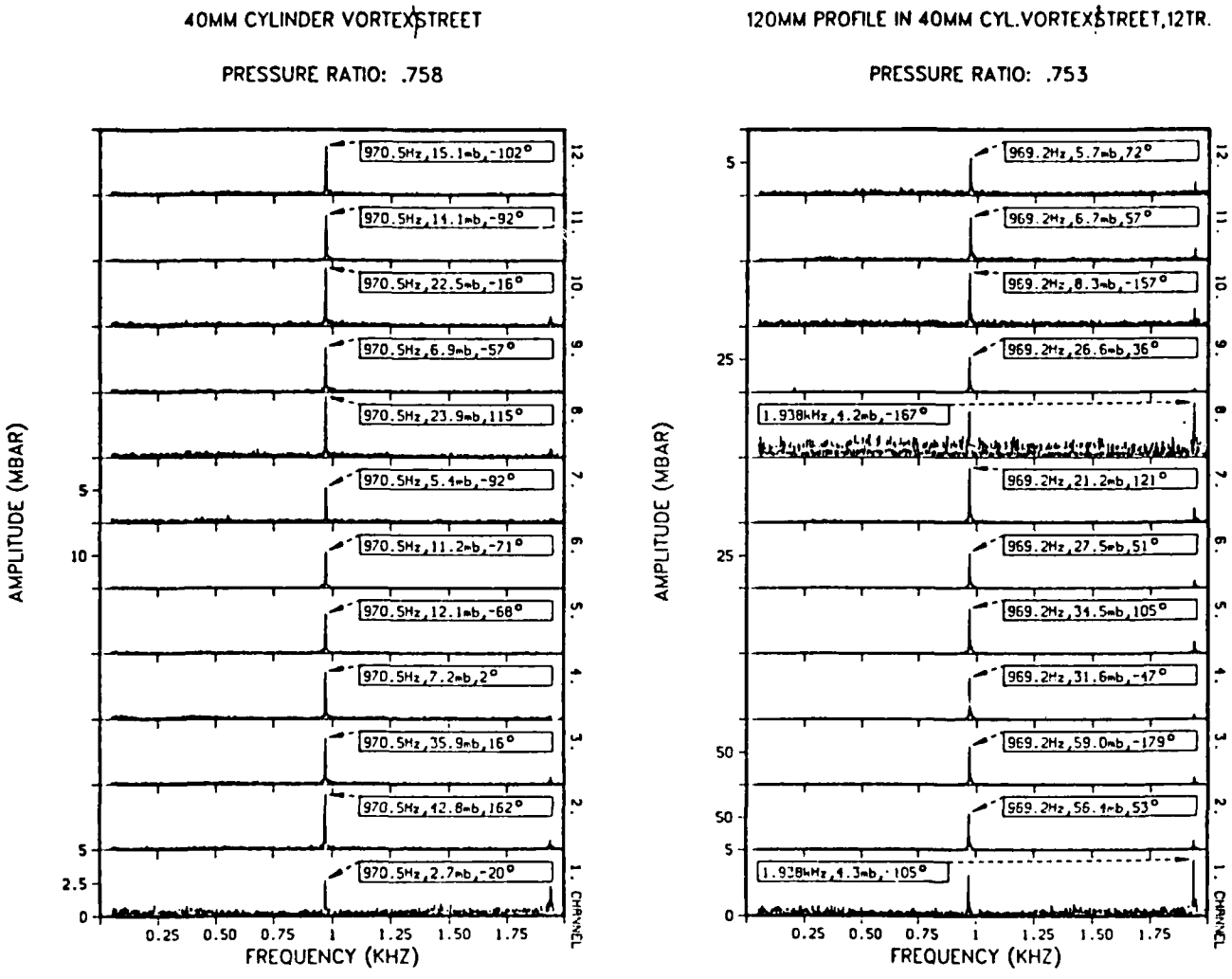

Figure 17a and 17b

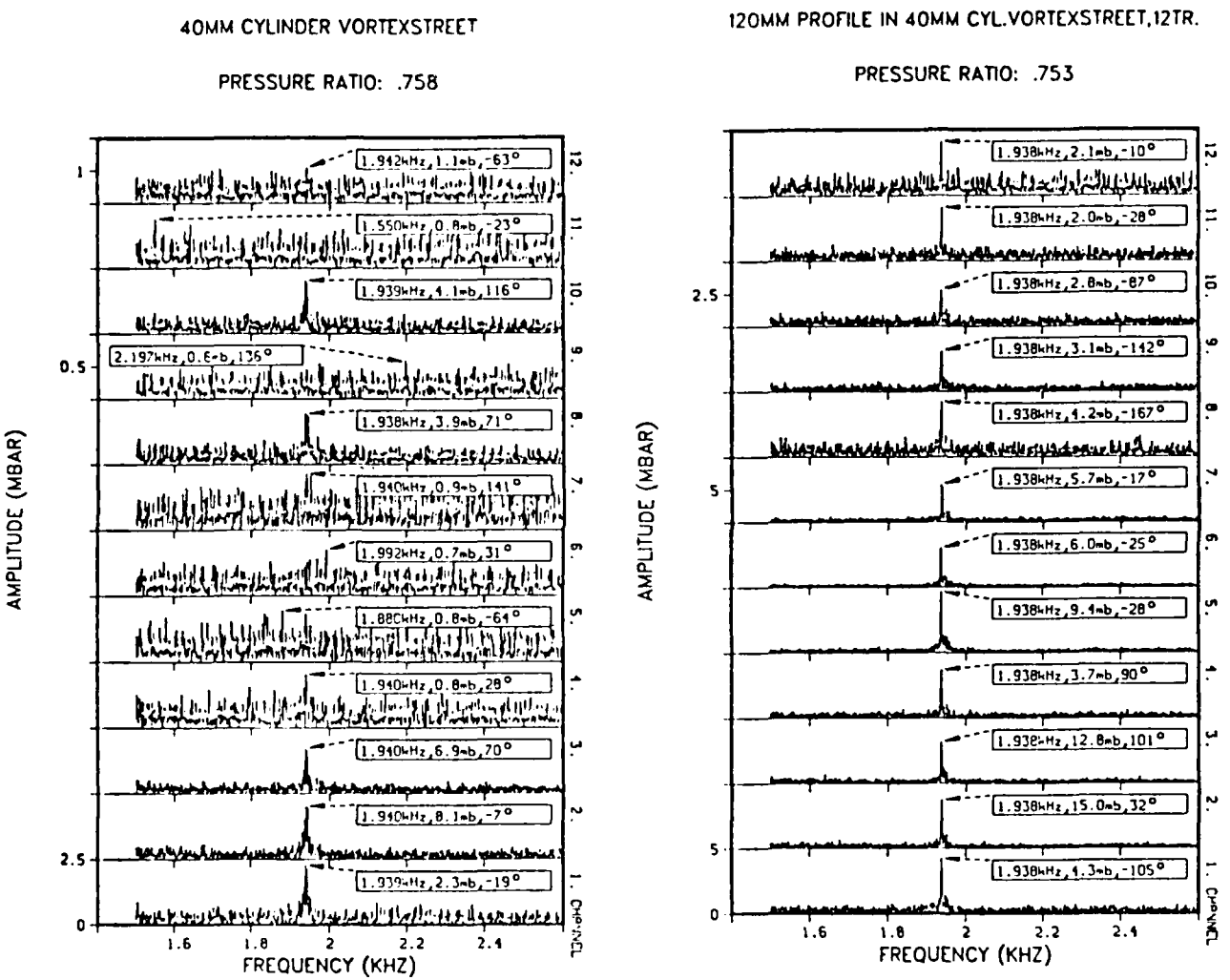

Figure 18a and 18b

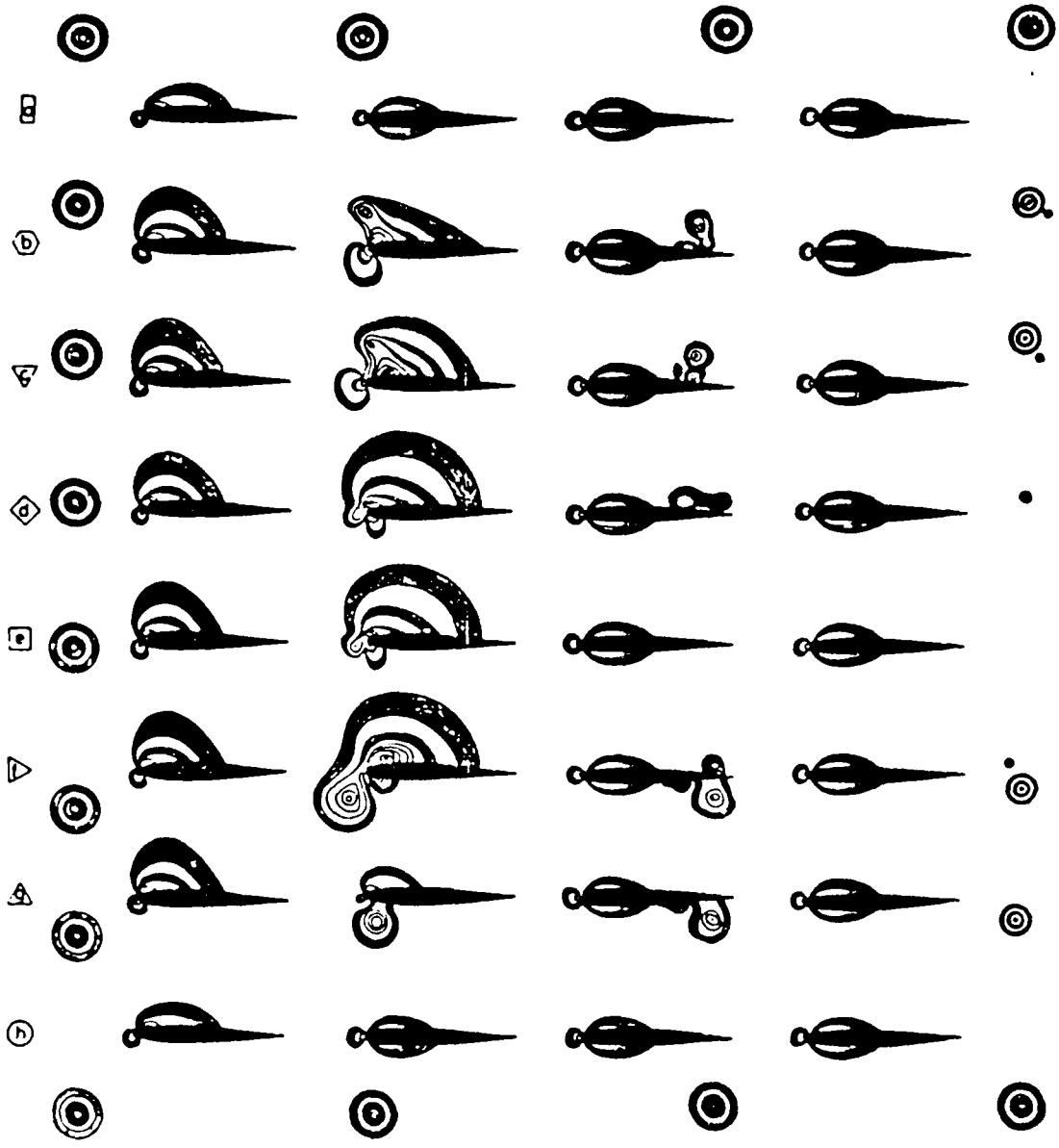

figure 19: 8 cases of vortex-airfoil interaction depending on flight height of the vortex.

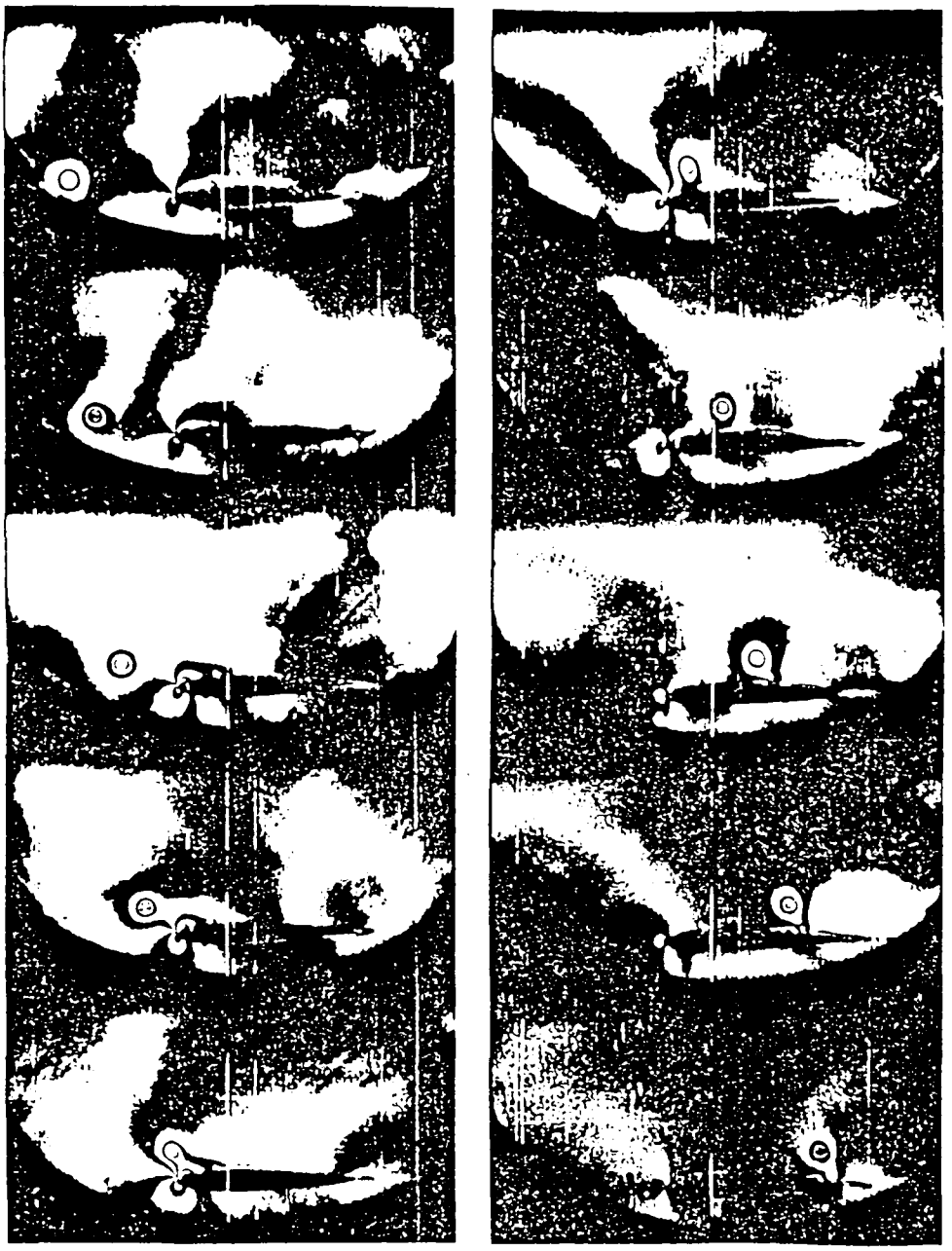

figure 20 Mach 0.2, Z = 0.5, Re = 290 000

figure 21: Ma = 0.8, Z = 0.7, Re 280 000

figure 22: Ma = 0.8, Z = 0.7, Re = 280 000

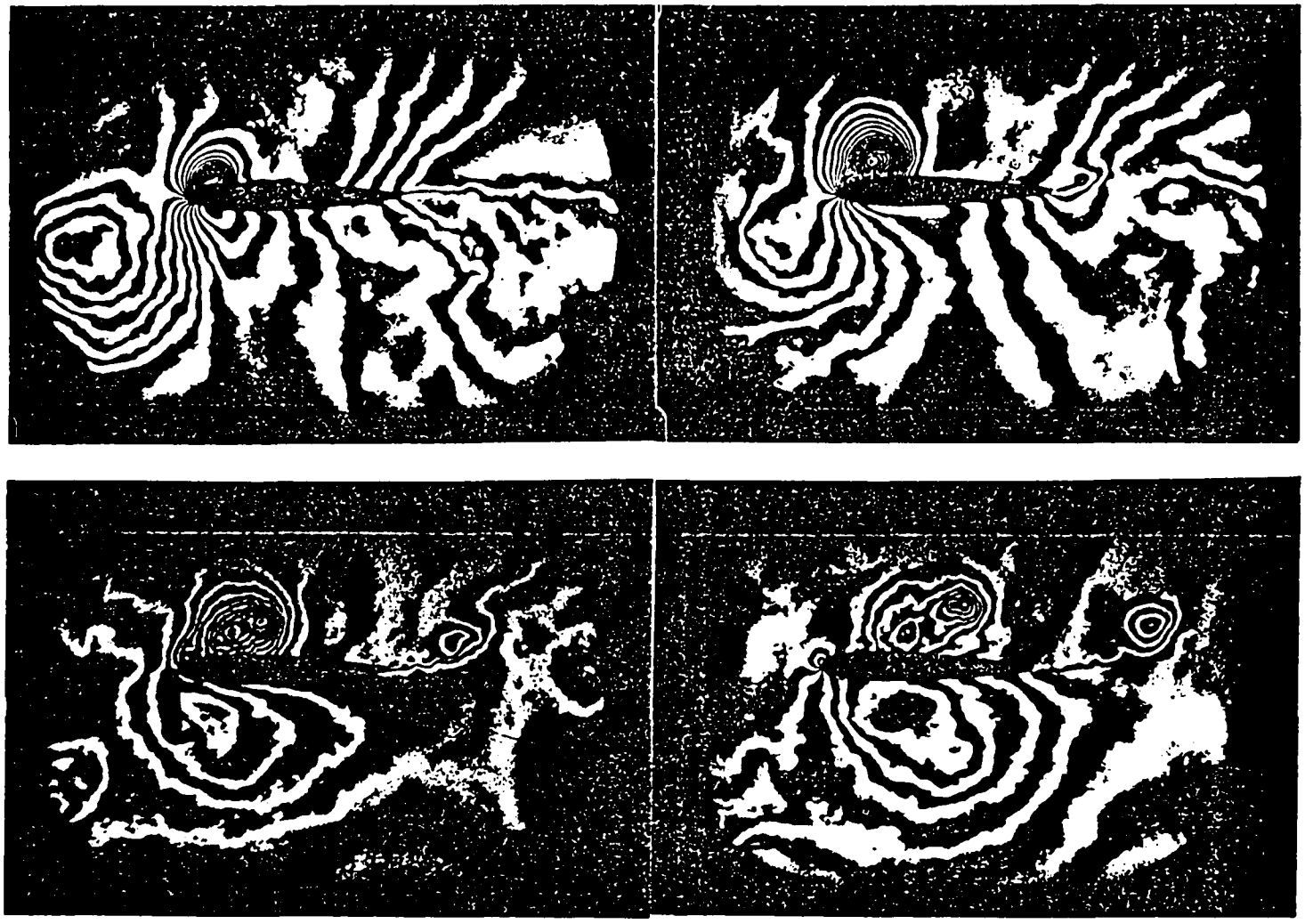

figure 23: M 0.25, Z = 4.0, Re = 340 000

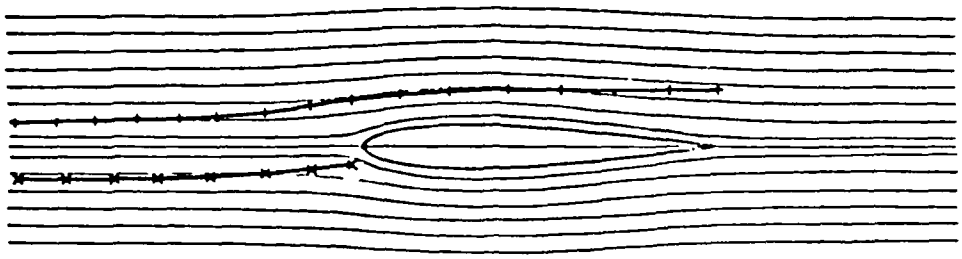

M = 0,2 , Re = 0,29 · 10^6 , Z = 0,25

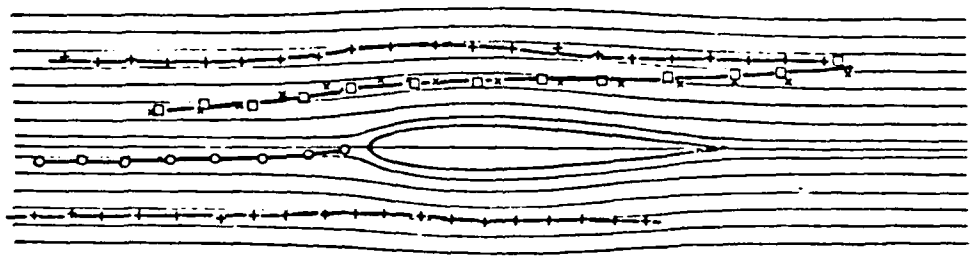

M = 0,2 , Re = 0,29 · 10^6 , Z = 0,5

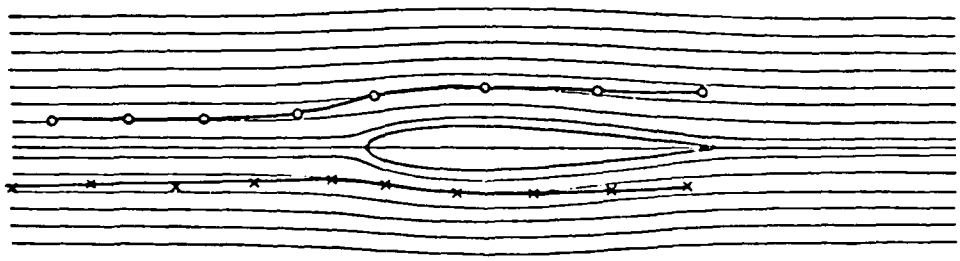

M = 0,4 , Re = 0,37 · 10^6 , Z = 0,4

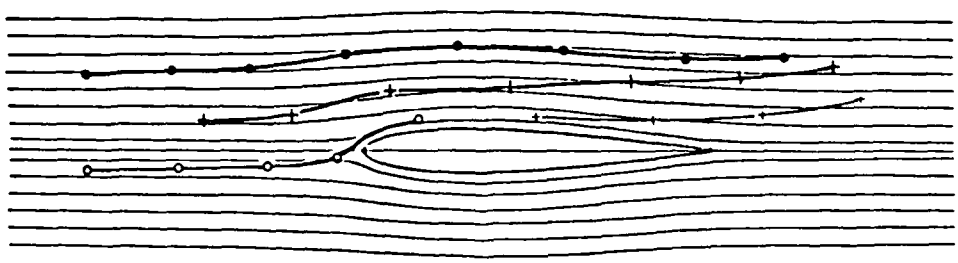

M = 0,4 , Re = 0,37 · 10^6 , Z = 0,65

Figure 24: Vortex paths (thick curves) curves and stream lines (thin curves).

Curve with crosses: secondary vortex

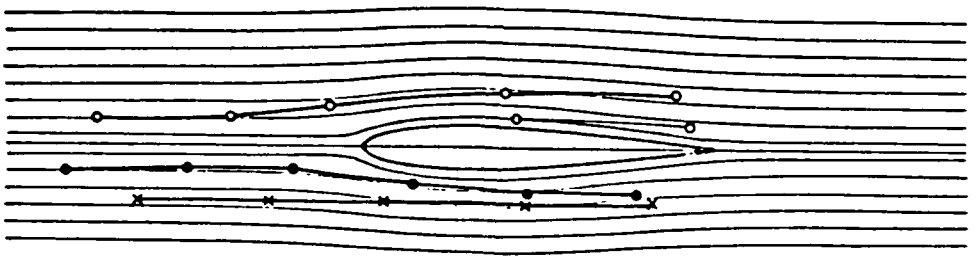

M = 0,6 , Re = 0,37 · 10^6 , Z = 0,4

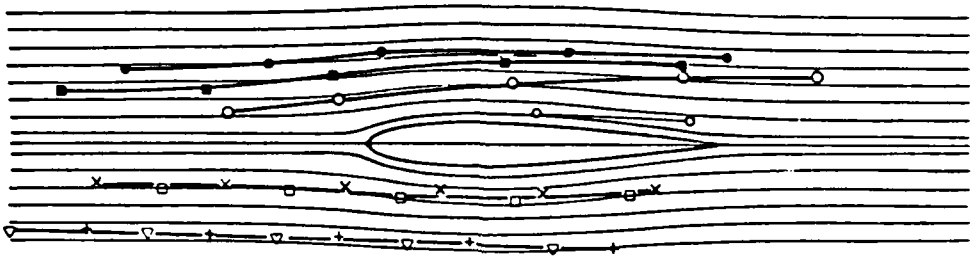

M = 0,6 , Re = 0,37 · 10^6 , Z = 0,7

Separate Linien bei M= 0,6 mit offenem Kreissymbol: Sekundärwirbel

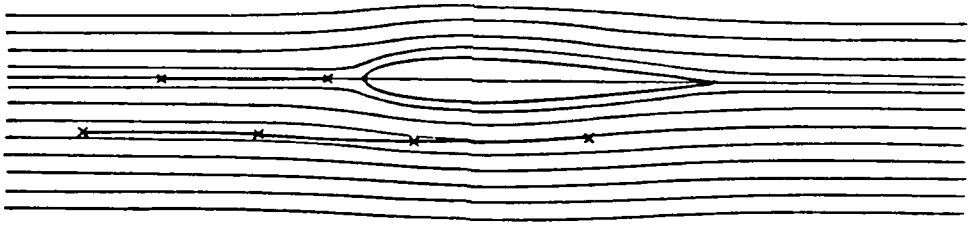

M = 0,8 , Re = 0,28 · 10^6 , Z = 0,3

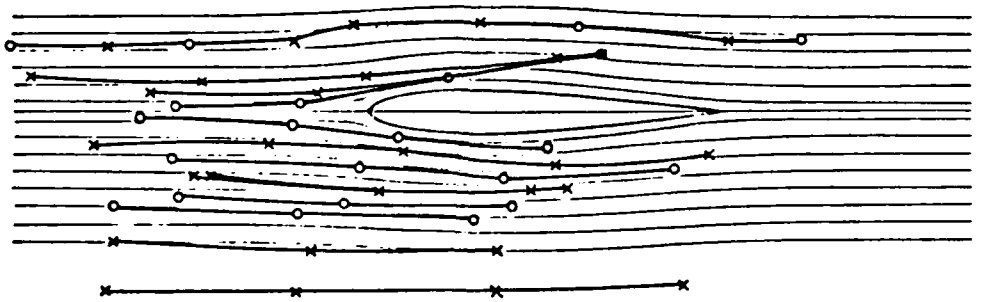

M = 0,8 , Re = 0,28 · 10^6 , Z = 0,7

Figure 25: Vortex paths (thick curves) and stream lines (thin curves).

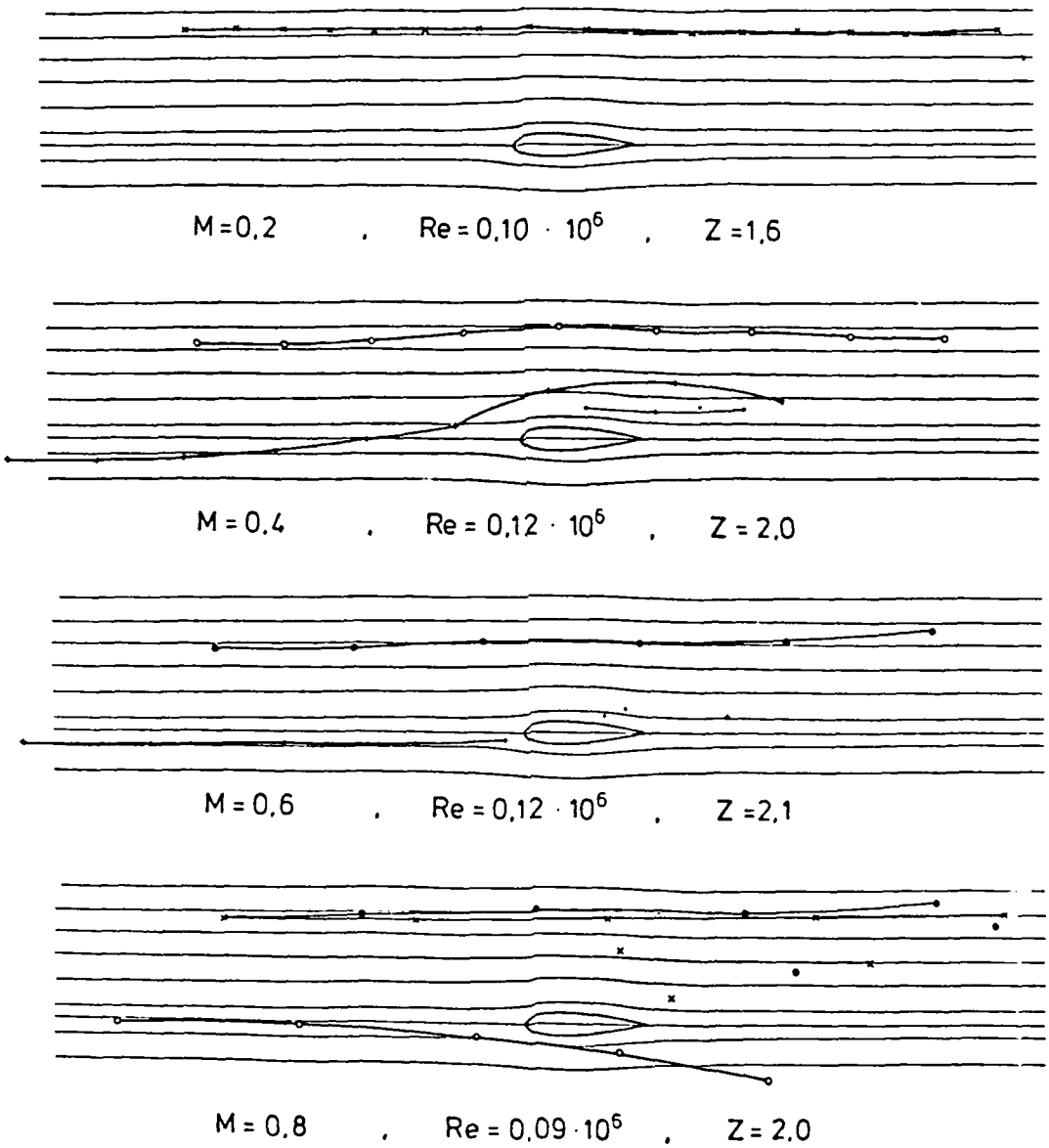

Figure 26: Paths of vortices with high coefficient of circulation.
Separate symbols: secondary vortices.

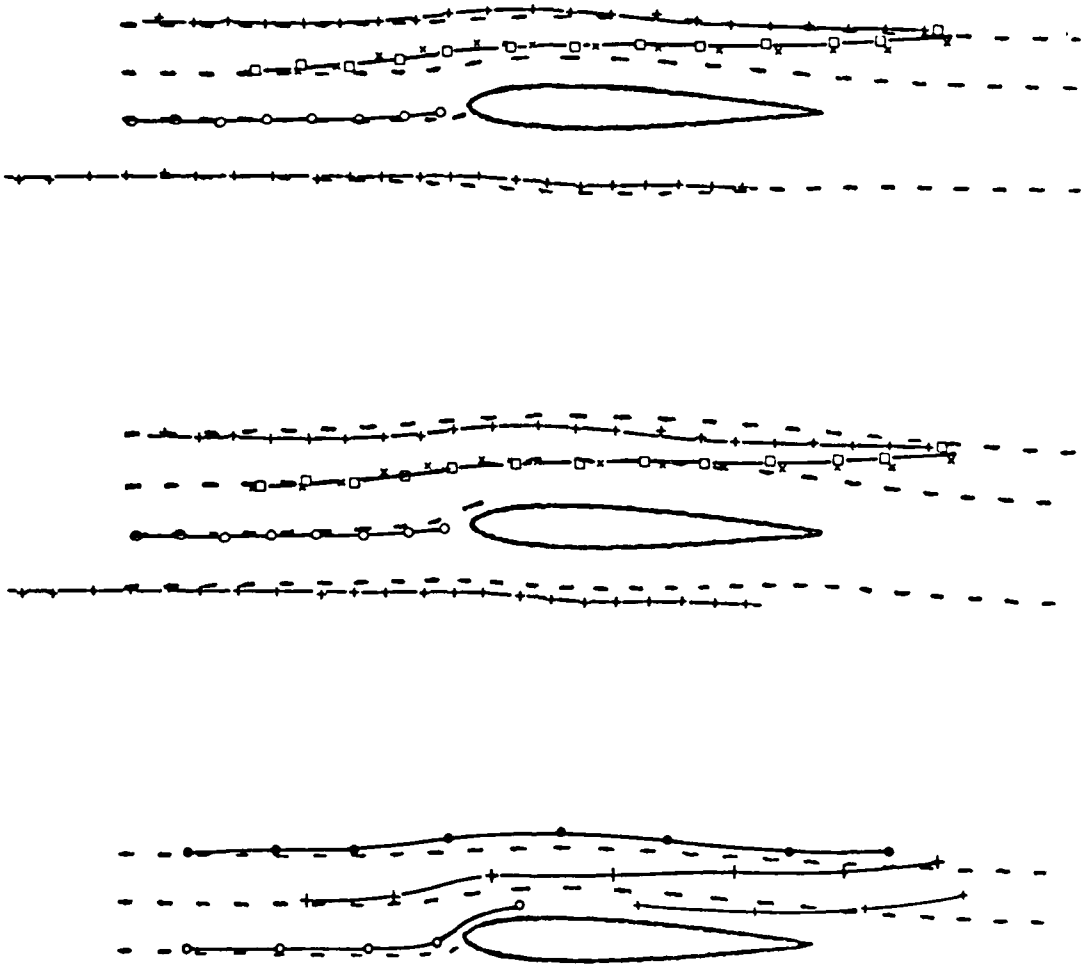

Figure 27: Calculated and measured paths.
Upper figure: Mach 0.2,
Re = 290 000, Z = 0.5
Middle figure: as in the first case but calculation done without the term corresponding to the central vortex.
Lower figure: Mach 0.4, Re = 370 000, Z = 0.65
Measured curves are solid.

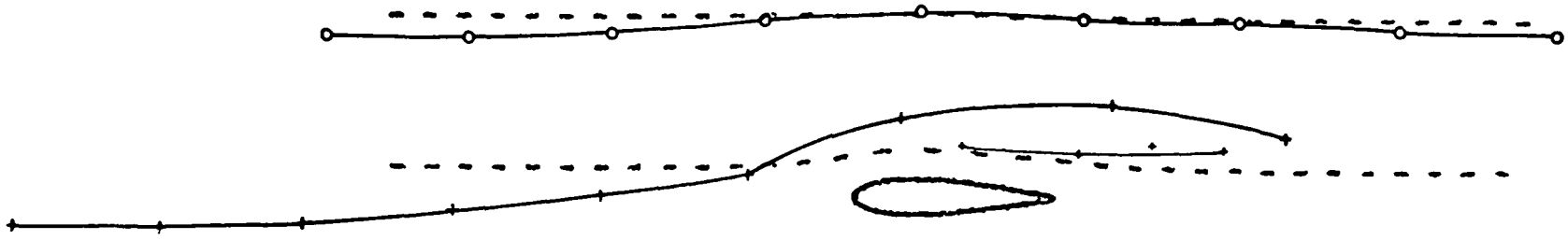

Figure 28: Measured (solid) and calculated paths
(same circulation and height of incoming vortex)
Mach 0.4, Re = 120 000, Z = 2.0

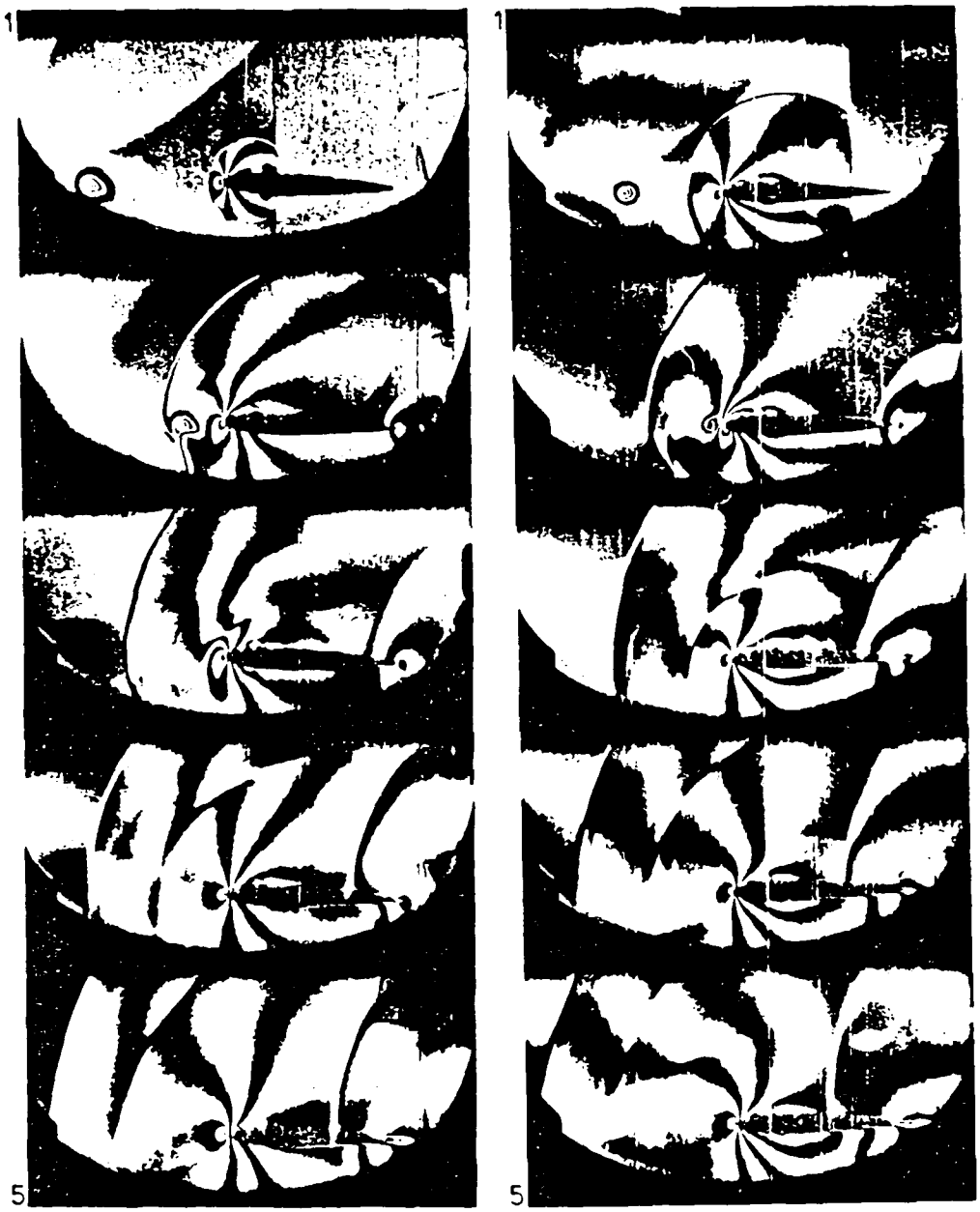

Figure 29a: 2 series of interferograms showing the generation of sound by a vortex directly hitting the leading edge.
Mach 0.8, Re = 280 000, Z = 0.3

Figure 29b: 2 series of interferograms showing the generation of sound by a vortex directly hitting the leading edge.
Mach 0.8, Re = 280 000, Z = 0.3

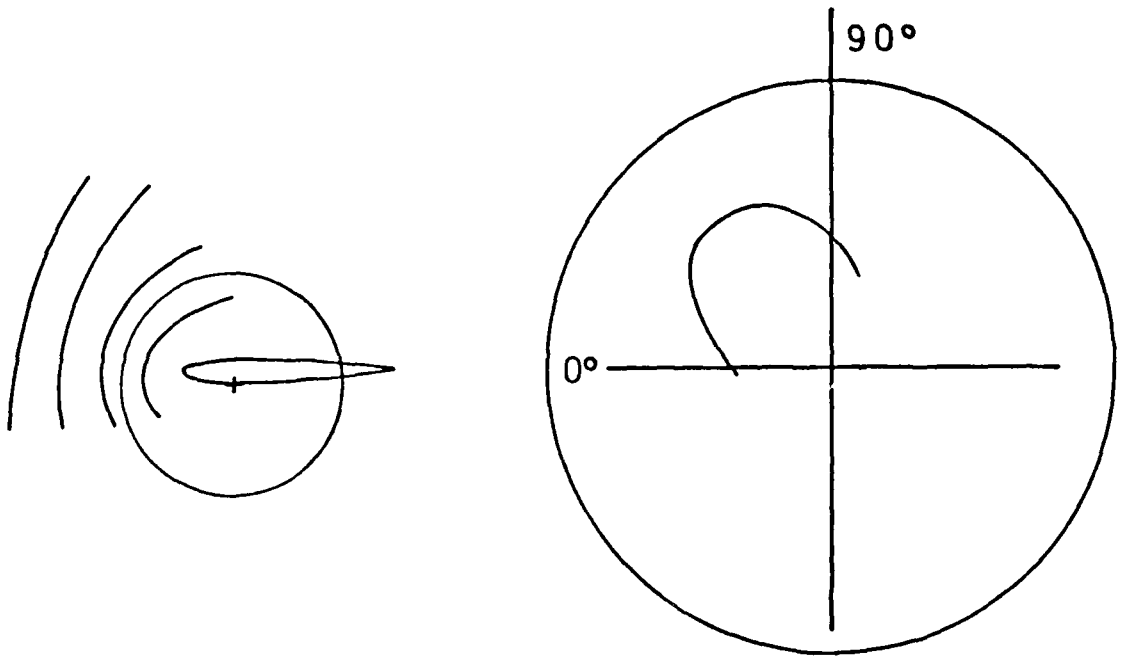

Figure 30: Left: Averaged development of the wavefronts in figure 29.
Right: Angular diagram of the density change of the compression wave for radius 0.5. Outer circle corresponds to one fringe (one third of stagnation pressure).

Figure 31: Generation of sound by vortices passing in different heights.
Mach 0.8, Re = 280 000, Z = 0.7.
Left series: h = 0.5; right series: h = 0.05.

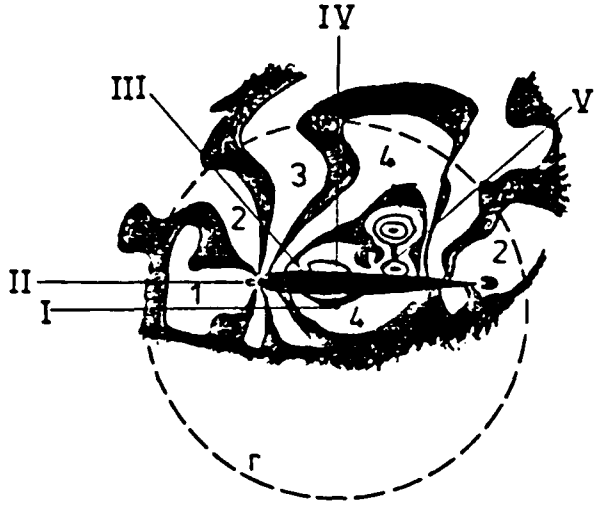

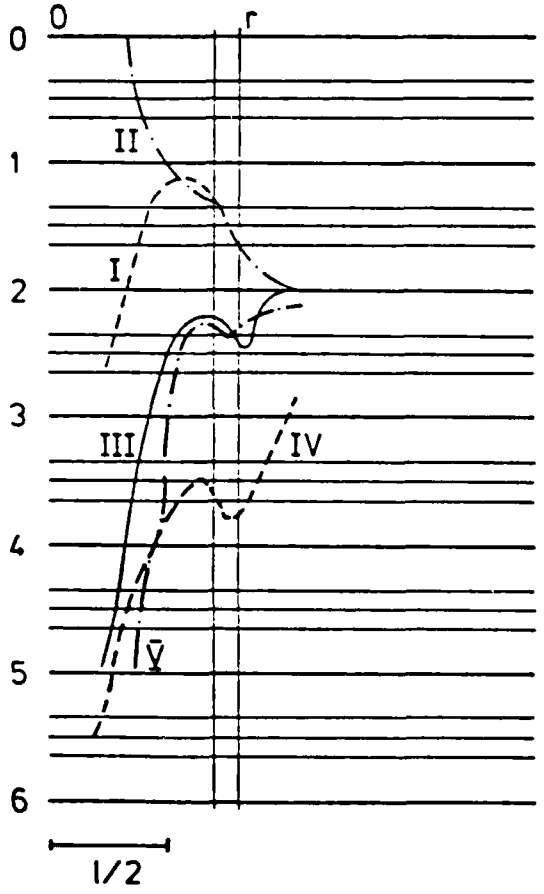

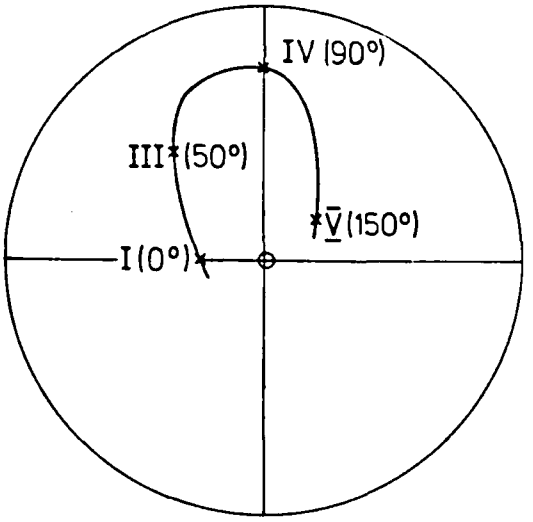

Figure 32a: Density along a line through the center of the wave; angular diagram for 31 (left series). Outer circle corresponds to one fringe (one third of stagnation pressure).

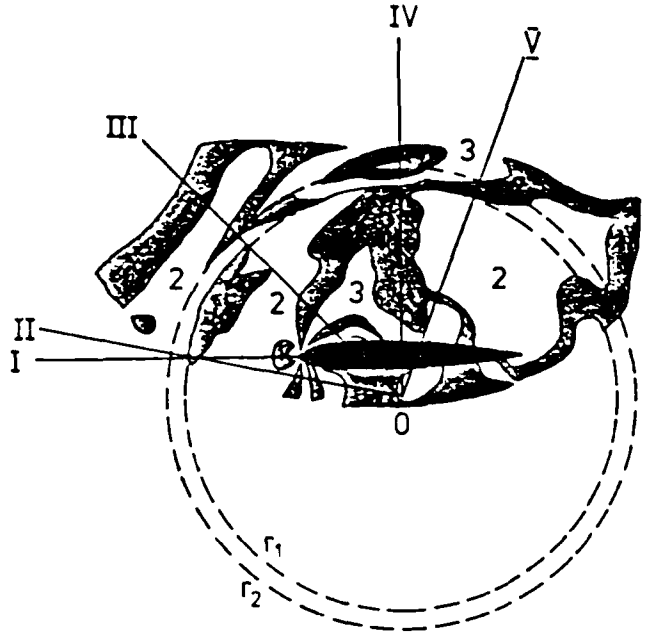

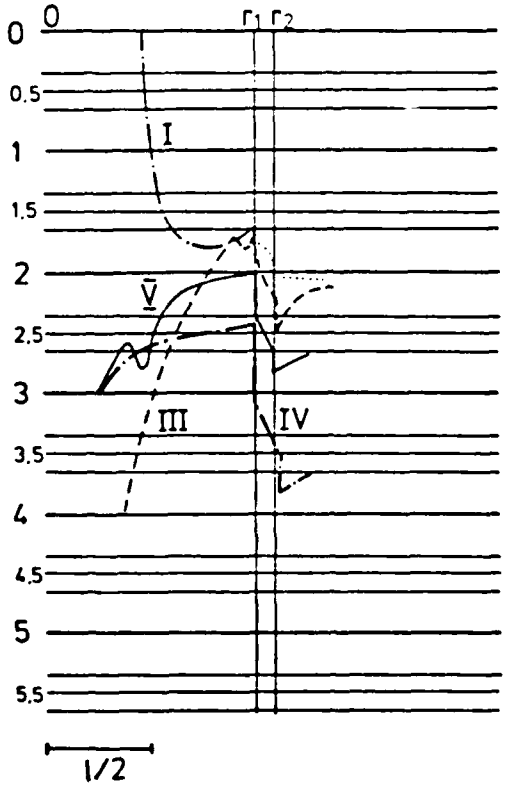

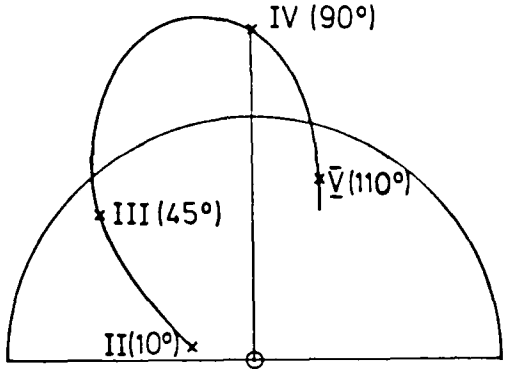

Figure 32b: Density along a line through the center of the wave; angular diagram for 31 (right series). Outer circle corresponds to one fringe (one third of stagnation pressure).

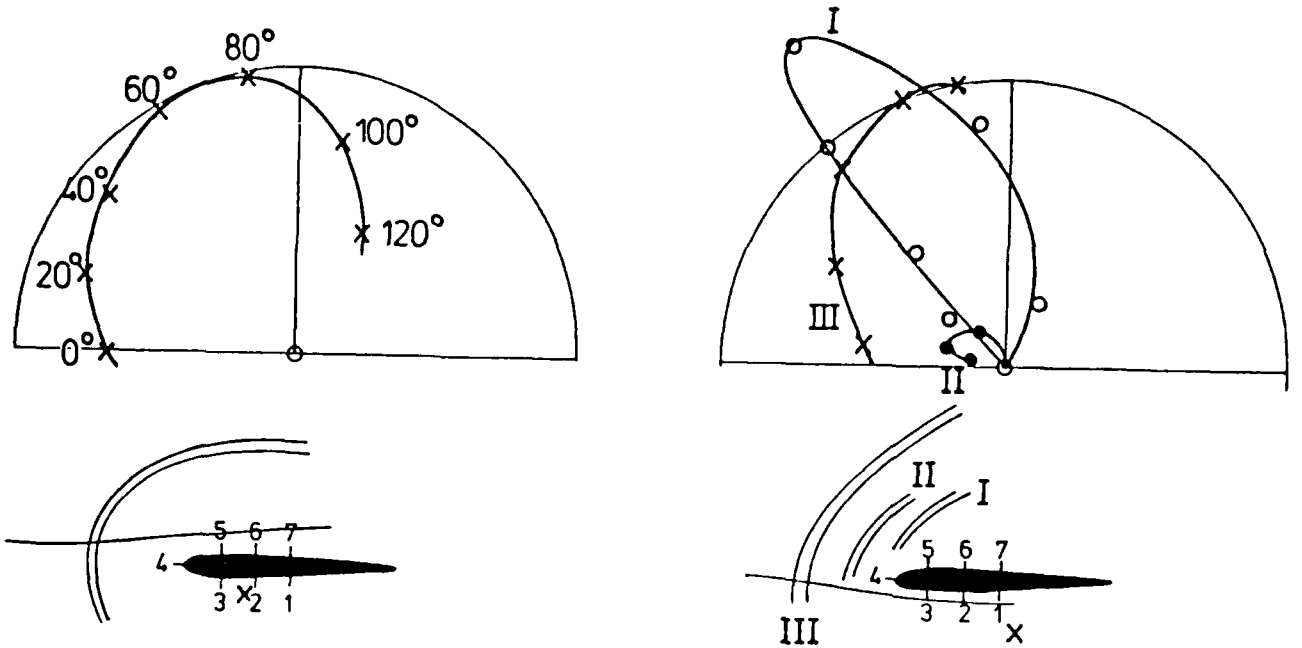

Figure 33: Wave fronts of figs. 21,22 and angular diagrams. Waves I,II of the third picture, III of the fourth. The center of the angular characteristic is indicated by the cross beneath the profiles. Thin curves show the vortex paths. Outer circle corresponds to one fringe (one third of stagnation pressure).

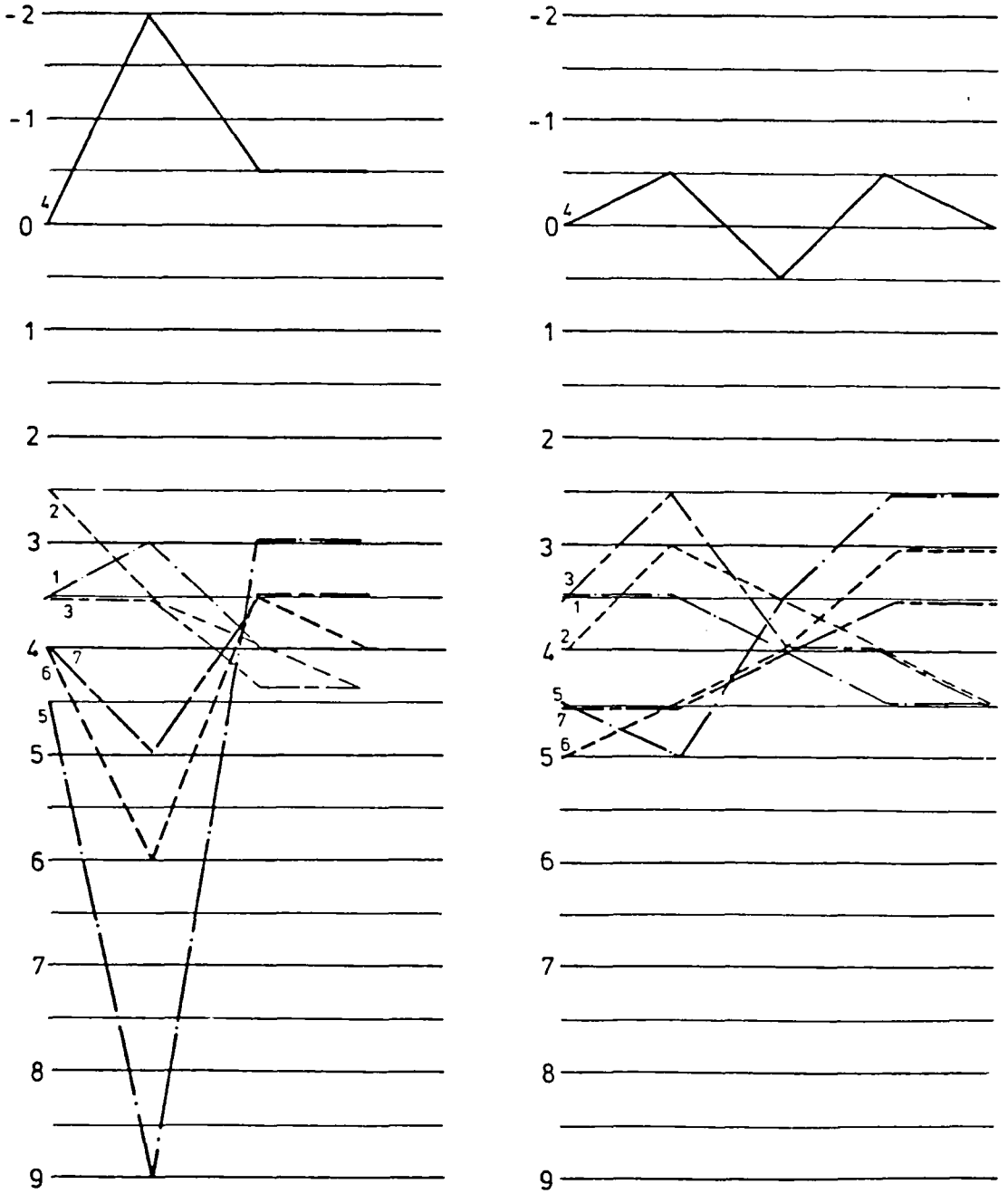

Figure 34: Fringe order at the surface of the profile (see figs. 21,22). The points 1-7 are indicated in figure 33. One fringe corresponds to one third of stagnation pressure.

a

b

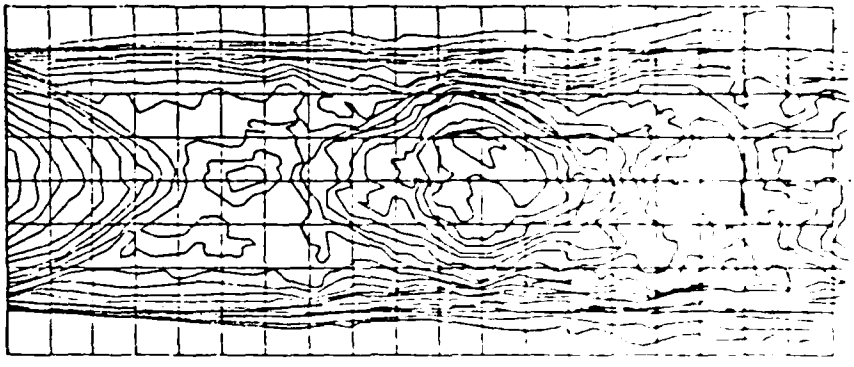

c

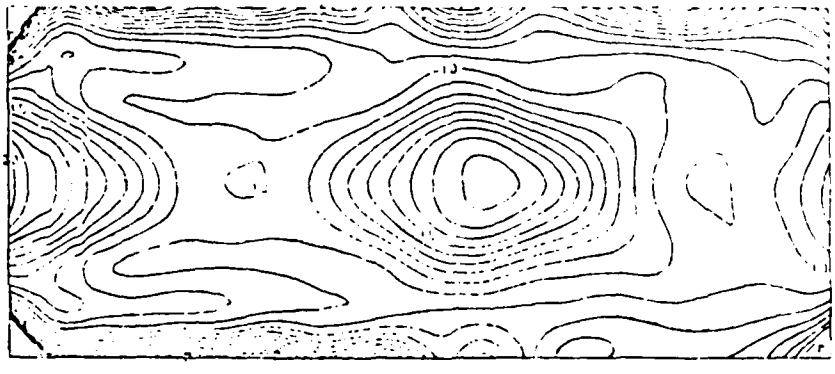

Figure 35: Example of interferogram averaging.

a) Interferogram of a supersonic stream.

b) Line pattern extracted from a)

c) Polynomial representation of 20 averaged pictures.

References

[1] Obermeier, F., On a new representation of aeroacoustic source distribution. I. Two-dimensional model flows, Acustica (1979) 42(1), 62-71

[2] Obermeier, F., On a new representation of aeroacoustic source distribution. II. Two-dimensional model flows, Acustica (1979) 42(1), 62-71

[3] Obermeier, F., The influence of solid boundaries on low Mach number vortex sound. Journal of Sound and Vibration (1980) 72(1), 39-49

[4] Walton, E.T.S., On the motion of vortices near a circular cylinder in a stream of liquid. Proceedings of the Royal Irish Academy (1928) 38, 29-39

[5] Lin, C.C., On the motion of vortices in two dimensions. Applied Mathematics Series No. 5. University of Toronto Studies.

[6] Parthasarathy, R., Aerodynamic sound generation due to vortex-aerofoil interaction. Dissertation Stanford University (1972)

[7] Routh, E.J., Some application of conjugate functions. Proceedings of the London Mathematical Society (1881) 12, 73-89

[8] Saffman, P.G. and Sheffield, J.S., Flow over a wing with an attached free vortex. Studies in Applied Mathematics (1977) 57, 107-117

[9] Huang, M.-K. and Chow, C.-Y., Trapping of a free vortex by Joukowsky airfoils. AIAA Journal (1982) 20(3), 292-298

[10] Obermeier, F., Effects of solid boundaries on aerodynamic sound generation. Max-Planck-Institut für Strömungsforschung (1979) Bericht 114/1979

[11] Obermeier, F., Zur aerodynamischen Schallerzeugung wirbelbehafteter Strömungen in der Umgebung starrer Körper. Max-Planck-Institut für Strömungsforschung (1978) Bericht 106/1978

[12] Meier, G.E.A., Ein instationäres Verhalten transsonischer Strömungen. Mitteilungen aus dem MPI für Strömungsforschung und der AVA (1974), Nr. 59

[13] Dosanjh, D.S., Weeks, T.M., Interaction of a starting vortex street with a travelling shock wave. AIAA Journal 3 (1965), 216

[14] Rehberg, I., Eine strömungsakustische Spitzenkatastrophe. Mitteilungen aus dem MPI für Strömungsforschung und der AVA (1983), Nr. 75

[15] Becker, F., Zur automatischen Auswertung von Interferogrammen. Mitteilungen aus dem MPI für Strömungsforschung (1982), Nrr. 74

[16] Becker, F., Meier, G.E.A. and Wegner, H., Automatic evaluation of interferograms. Applications of Digital Image Processing IV, Andrew G. Tescher, Ed., Proc. SPIE 359 (1982), 386-393

[17] Drawing contours from arbitrary data points. The Computer Journal 17, No. 4 (1974), 318-324

[18] Lindblad, I., The effect on acoustic radiation of mutual interaction between a line vortex and an airfoil. Flygtekniska Försöksanstalten Stockholm (1983) FFA TN 1983-45

[19] Meier, G.E.A., Timm, R., Becker, F., Initial experiments on profile-vortex interaction. Max-Planck-Institut für Strömungsforschung (1983) Bericht 6/1983

END

12-86

DTIC